



Importance of Resolving Kuroshio Front and Eddy Influence in Simulating the North Pacific Storm Track

XIAOHUI MA

Physical Oceanography Laboratory, Qingdao Collaborative Innovation Center of Marine Science and Technology, Ocean University of China, Qingdao, China, and Department of Oceanography, Texas A&M University, College Station, Texas

PING CHANG

Department of Oceanography, and Department of Atmospheric Sciences, Texas A&M University, College Station, Texas, and Physical Oceanography Laboratory, Qingdao Collaborative Innovation Center of Marine Science and Technology, Ocean University of China, Qingdao, China

R. SARAVANAN AND RAFFAELE MONTUORO

Department of Atmospheric Sciences, Texas A&M University, College Station, Texas

HISASHI NAKAMURA

Research Center for Advanced Science and Technology, University of Tokyo, Tokyo, Japan

DEXING WU, XIAOPEI LIN, AND LIXIN WU

Physical Oceanography Laboratory, Qingdao Collaborative Innovation Center of Marine Science and Technology, Ocean University of China, Qingdao, China

(Manuscript received 23 February 2016, in final form 5 November 2016)

ABSTRACT

Local and remote atmospheric responses to mesoscale SST anomalies associated with the oceanic front and eddies in the Kuroshio Extension region (KER) are studied using high- (27 km) and low-resolution (162 km) regional climate model simulations in the North Pacific. In the high-resolution simulations, removal of mesoscale SST anomalies in the KER leads to not only a local reduction in cyclogenesis but also a remote large-scale equivalent barotropic response with a southward shift of the downstream storm track and jet stream in the eastern North Pacific. In the low-resolution simulations, no such significant remote response is found when mesoscale SST anomalies are removed. The difference between the high- and low-resolution model simulated atmospheric responses is attributed to the effect of mesoscale SST variability on cyclogenesis through moist baroclinic instability. It is only when the model has sufficient resolution to resolve small-scale diabatic heating that the full effect of mesoscale SST forcing on the storm track can be correctly simulated.

1. Introduction

It has been recognized for decades that for basin-scale air–sea interactions in midlatitudes, coupling between the atmosphere and ocean is largely linear and passive in nature (Barsugli and Battisti 1998; Frankignoul 1985). In

this passive air–sea coupling, the ocean responds to white-noise atmospheric internal variability through turbulent air–sea heat fluxes, giving rise to a red-noise response in sea surface temperature (SST; Frankignoul and Hasselmann 1977; Hasselmann 1976), and the atmosphere in turn experiences reduced surface thermal damping due to the SST adjustment, causing enhancement in low-frequency atmospheric variance (Barsugli and Battisti 1998; Kushnir et al. 2002). This type of

Corresponding author e-mail: Xiaohui Ma, maxiaohui@tam.u.edu

passive air–sea coupling appears to prevail in most areas of midlatitudes (Mantua et al. 1997; Okumura et al. 2001; Xie 2004) with the exception of western boundary regimes, such as the Kuroshio and Gulf Stream, where atmosphere–ocean feedback can take an active form. In fact, extensive research in past decades shows that it is the active atmosphere–ocean feedback along western boundary regimes that can exert a significant influence on midlatitude atmospheric storm tracks (Bryan et al. 2010; Kelly et al. 2010; Kushnir et al. 2002; Kwon et al. 2010; Miller and Schneider 2000).

Unlike the passive air–sea coupling, the active atmosphere–ocean feedback is nonlinear and mediated by baroclinic eddies (Bryan et al. 2010; Kushnir et al. 2002; Small et al. 2008; Taguchi et al. 2012; Nonaka et al. 2016). Quantifying and understanding the underlying mechanisms have proven to be a formidable challenge because 1) western boundary current regimes are one of the most active regions of the climate system where both the atmosphere and ocean are dynamically unstable, producing energetic eddies that tend to mask the ocean–atmosphere feedback governed by strong SST gradients' influence on atmospheric baroclinicity and 2) the interaction in western boundary current regimes takes place at frontal scale and mesoscale where until recently available observations and numerical modeling tools have been inadequate to resolve these small-scale dynamical processes. As a result, detailed mechanisms governing air–sea interaction along western boundary current regimes are still lacking.

Many recent studies on extratropical active air–sea feedback draw attention to the influence of the strong SST gradient in western boundary regimes on lower-atmospheric baroclinicity by investigating the sensitivity of atmospheric response to the sharpness of the SST gradient along oceanic fronts or to the shift of oceanic fronts. Brayshaw et al. (2008) showed that an intensified midlatitude SST gradient can give rise to a stronger and poleward shift of midlatitude storm tracks [by the measure of 2–6-day bandpass-filtered geopotential height (GPH) variance] in an idealized atmospheric general circulation model (AGCM) simulation. Suppression of the sharp SST gradient in frontal regions, on the other hand, can lead to an equatorward shift of the entire low-level atmospheric circulation system, including the surface westerlies, jet streams, and subtropical high pressure belt (Sampe et al. 2010). By comparing atmosphere-only model simulations forced by prescribed SSTs, Taguchi et al. (2009) showed a reduced storm-track activity in response to a weakened SST gradient forcing due to the decreased meridional gradient of turbulent heat fluxes and moisture fluxes across the oceanic front. Small et al. (2014) reported a similar finding along the Gulf Stream and Southern Ocean fronts based

on a high-resolution (~ 50 km) AGCM study. Joyce et al. (2009) showed that shifts in the Kuroshio and Gulf Stream at interannual and decadal time scales may produce a meridional shift in local storm-track position or even a nonlocal downstream response. Frankignoul et al. (2011) reported a large-scale atmospheric circulation response that resembles the North Pacific Oscillation (NPO) pattern to a meridional shift of the Kuroshio–Oyashio front. More recently, O'Reilly and Czaja (2015) identified a response of the North Pacific storm track to SST anomalies associated with the variability of the Kuroshio Extension. Some of the recent progress in understanding the role of the sharp SST gradient along oceanic fronts in large-scale atmospheric circulation can be found in recent reviews (Kelly et al. 2010; Kwon et al. 2010).

In addition to SST gradient effects, it has been shown convincingly that mesoscale SST anomalies associated with energetic ocean eddies in western boundary regimes can have a distinct impact on atmospheric boundary layer. High-resolution satellite observations reveal that mesoscale SST anomalies along oceanic fronts can force a well-defined mesoscale near-surface wind response (Chelton and Xie 2010; Chelton et al. 2004). By spatially filtering the high-resolution satellite SST and surface wind stress (speed), a positive correlation has been revealed between mesoscale SSTs and surface winds: warm (cold) ocean eddies tend to correspond to stronger (weaker) surface wind speed anomalies. Using a fully coupled regional ocean–atmosphere model configured for the Kuroshio Extension region (KER), Putrasahan et al. (2013) recently reproduced the observed coupling strength between mesoscale SSTs and surface winds, as well as the coupling between the SSTs and surface heat fluxes. Putrasahan et al.'s (2013) results confirm previous findings that surface turbulent heat fluxes along oceanic fronts tend to damp mesoscale SST anomalies (Bryan et al. 2010; Haack et al. 2005; Seo et al. 2007) and that ocean forcing atmosphere prevails at mesoscales. They also showed that surface wind convergence driven by mesoscale SST gradients can produce a precipitation response along the KER, suggesting a deep tropospheric response to mesoscale SSTs. Similar rainfall response is also revealed in satellite observations by Frenger et al. (2013), who found that warm (cold) oceanic eddies tend to be paired with intensified (weakened) local convection and positive (negative) rainfall anomalies in the Southern Ocean. Masunaga et al. (2016) further confirmed these atmospheric boundary layer responses to SST anomalies associated with the interannual variability of the Kuroshio Extension using satellite and reanalysis data. A review of the recent progress in our understanding of frontal

and mesoscale air–sea interactions is given by [Small et al. \(2008\)](#).

Besides the well-established local impact, the potential role of mesoscale SSTs in forcing atmospheric storm tracks and producing remote basin-scale atmospheric response has been highlighted by recent high-resolution climate model studies. [Small et al. \(2014\)](#) and [Piazza et al. \(2016\)](#) both noted a shift of lower- and upper-level storm track in their respective high-resolution global climate model simulations after removing the frontal and mesoscale SST anomalies in the Gulf Stream region. This North Atlantic storm track and mean flow response to mesoscale SST forcing in the Gulf Stream region was attributed to Rossby wave breaking as suggested by [Piazza et al. \(2016\)](#). [Zhou et al. \(2015\)](#), on the other hand, highlighted the importance of high-frequency (daily) SSTs in driving the North Pacific atmospheric variability using a T213 spectral resolution ($\sim 0.56^\circ$) AGCM. More recently, [Ma et al. \(2015\)](#) investigated the remote impact of mesoscale SST variability along the KER on the Pacific storm track using a high-resolution ($\sim 0.25^\circ$) regional climate model. Suppressing mesoscale SST variability, [Ma et al.'s \(2015\)](#) model simulations revealed a robust equivalent barotropic response in the eastern North Pacific accompanied by a significant shift in the storm track and winter rainfall variability along the U.S. West Coast. By diagnosing baroclinic eddy energetics, [Ma et al. \(2015\)](#) identified the importance of moist diabatic processes in mediating the effect of mesoscale SSTs on cyclogenesis and storm track through the so-called moist baroclinic instability ([Ahmadi-Givi et al. 2004](#); [Emanuel et al. 1987](#); [Lapeyre and Held 2004](#)). This finding is consistent with a recent study by [Willison et al. \(2013\)](#), which highlighted the importance of explicitly resolving moist diabatic processes in simulating North Atlantic cyclogenesis and storm track.

The present study attempts to extend the study by [Ma et al. \(2015\)](#) by further exploring the importance of resolving the Kuroshio Front and eddy influences in simulating the North Pacific storm track. Following the approach by [Willison et al. \(2013\)](#), we will compare high- and low-resolution regional climate model simulations with and without mesoscale SST forcing in the North Pacific. The scientific questions to be addressed are the following: 1) How do the local and remote atmospheric response to mesoscale SST anomalies in the KER differ between high- and low-resolution models? 2) What is the underlying dynamics responsible for the difference in local and remote storm-track response?

This paper is organized as follows. [Section 2](#) describes the model setup and experiment design. [Section 3](#) validates model simulations against observations. [Section 4](#) compares the local and remote atmospheric response to

mesoscale SST forcing between high- and low-resolution model simulations. [Section 5](#) examines the dynamic mechanisms of mesoscale-SST-induced storm-track response and mean flow changes in the North Pacific. Finally, a summary of major findings and discussion are presented in [section 6](#).

2. Regional climate simulations

a. Model configuration

Similar to [Ma et al. \(2015\)](#) and [Willison et al. \(2013\)](#), in this study we use the Weather Research and Forecasting (WRF) Model developed by NCAR ([Skamarock et al. 2008](#)). The model setup follows [Ma et al. \(2015\)](#) closely, and a brief description of the model is given below for completeness. The computational domain covers the entire North Pacific from 3.6° to 66°N and from 99° to 270°E with top of the atmosphere at 10 hPa and 30 vertical levels for all simulations. The model configuration includes the Kain–Fritsch (KF) cumulus scheme ([Kain 2004](#)), [Lin et al.'s \(1983\)](#) microphysics scheme, the Noah land surface scheme, the YSU planetary boundary layer (PBL) scheme ([Hong and Pan 1996](#)), and the RRTM for GCMs (RRTMG) and Goddard scheme for longwave and shortwave radiation ([Chou and Suarez 1994](#); [Mlawer et al. 1997](#)). A more detailed description of the model configuration and parameterization schemes applied in our simulation can be found in [Ma et al. \(2015\)](#).

In all the simulations, microwave infrared optimal interpolated (MW-IR; 2002–present) daily SST provided by Remote Sensing Systems (RSS) with a horizontal resolution of 0.09° (about 10 km) is used as the lower boundary forcing for WRF. This SST dataset has sufficient spatial resolution to resolve mesoscale SST variability associated with oceanic eddies in the KER. The experiment period is from 1 October 2007 to 31 March 2008 for WRF, so that the SST forcing along with the initial and lateral boundary conditions derived from 6-hourly NCEP–DOE AMIP-II reanalysis (NCEP-2) data ([Kanamitsu et al. 2002](#)) are all set for this time period. The 2007/08 winter is chosen because the Kuroshio was in an unstable state during this period ([Qiu et al. 2014](#)), and thus eddy activity was strong. At the same time, it was a relatively neutral ENSO and PDO year, which helps to minimize the influence from the large-scale climate modes of variability on the North Pacific storm track.

b. Experiment design

Throughout the study, we carry out twin ensembles of WRF simulations with two different spatial resolutions. The high-resolution simulations use a horizontal

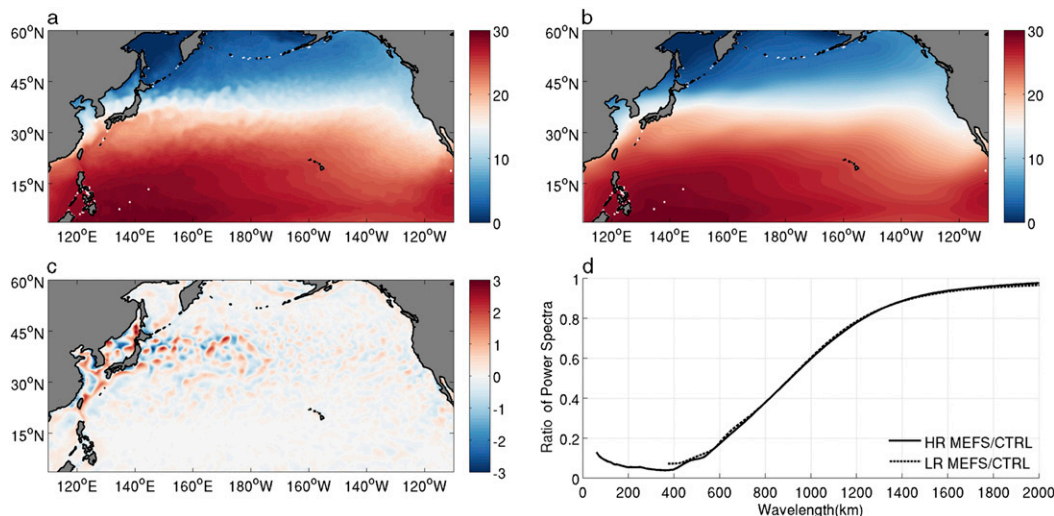


FIG. 1. Winter season (NDJFM) mean SST ($^{\circ}\text{C}$) in (a) HR-CTRL and (b) HR-MEFS and (c) the difference between them. (d) Ratio (MEFS/CTRL) of SST power spectra computed in the KER (27° – 42°N , 155°E – 180°) for high- (solid) and low-resolution (dash) simulations.

resolution of 27 km, while the low-resolution simulations use a 162-km grid that is 6 times coarser than the high-resolution grid and is comparable to the typical resolution of global climate models (at $\sim\text{T85}$ spectral resolution). According to Willison et al. (2013), at ~ 20 -km resolution, models begin to explicitly resolve the diabatic heating structure during cyclogenesis. Each of the twin ensembles contains 10 members with different initial conditions generated by using the reanalysis data on 1 October of 10 different years (i.e., 2002, 2003, ..., 2011) but with identical lateral boundary conditions for the 2007/08 winter. We note that the ensemble size of 10 may not be large by global AGCM standards. However, the use of the identical lateral boundary conditions in the regional modeling approach effectively enhances the signal-to-noise ratio compared to the same size of AGCM ensemble simulations because remote influences from the other regions, including the tropics, are eliminated by the regional modeling approach. The only difference between the two ensembles of runs is the SST forcing field: one ensemble is forced with the high-resolution MW-IR SST [referred to as control simulations (CTRL)], while the other is forced with a low-pass spatially filtered MW-IR SST to remove mesoscale SSTs [referred to as mesoscale-eddy-filtered simulation (MEFS)]. A Loess spatial filter was applied to the MW-IR SST, with a 15° (longitude) \times 5° (latitude) cutoff wavelength (Schlax and Chelton 1992). Figures 1a–c illustrate the original and filtered winter season mean SST employed in CTRL and MEFS, as well as the difference between the two. As can be seen, most of the mesoscale SST features removed by the filter are confined to the

eddy-rich region along the KER where we expect the most intense air–sea coupling to occur and mesoscale SST anomalies in the tropics are negligibly weak compared to those in the midlatitude. The ratio between the filtered and unfiltered SST spectrum in the KER (Fig. 1d) further shows that the half-power wavelength of the mesoscale SSTs removed by the Loess filter is approximately 900 km for both the 27- and 162-km experiments (although the 162-km experiments can only resolve SST with spatial scale larger than 350 km), confirming that the removed SST variance is mostly at mesoscales. Comparison of the twin ensembles can help us to understand the effect of mesoscale SSTs associated with oceanic front and eddies in the KER on the atmosphere in the North Pacific. In the following discussion, we refer to 27-km twin ensembles as high-resolution CTRL (HR-CTRL) and MEFS (HR-MEFS), respectively, and 162-km twin ensembles as low-resolution CTRL (LR-CTRL) and MEFS (LR-MEFS), respectively.

It is worth emphasizing that LR-CTRL and LR-MEFS are identical to HR-CTRL and HR-MEFS, respectively, except for the horizontal resolution difference. In the high-resolution experiment, the 0.09° MW-IR SST was regridded onto the 27-km model grids to force WRF. In the low-resolution experiment, the SST from high-resolution model grids (27 km) was regridded onto the low-resolution model grid (162 km). Because of the regridding, the resultant SST variance, particularly over the KER, is different with a lower value for the low-resolution grid than the high-resolution grid. This is simply due to the fact that the low-resolution grid does

not fully retain mesoscale SST variability in the MW-IR data. It raises an issue concerning whether the different atmospheric response in high- and low-resolution simulations can be caused merely by the difference in the amplitude of the SST forcing or by the difference in the adequacy of resolving moist diabatic processes. To address this issue, we carry out another sensitivity experiment where mesoscale SST forcing for the low-resolution WRF is strengthened by a factor of 1.5. Specifically, this is done as follows: first, high-pass- and low-pass-filtered SSTs are derived using the Loess filter on the 27-km-grid SST; then these filtered SSTs are regridded onto the 162-km WRF grid; and finally the regridded high-pass SSTs are multiplied by a factor of 1.5 and added onto the regridded low-pass SST to form a new SST forcing for the low-resolution WRF. We refer to this ensemble of runs as the modified low-resolution control simulations (M-LR-CTRL).

c. Significance test

A two-sided Wilcoxon rank sum test is used to test statistical significance of the difference between the twin ensembles in the following analysis. The prime reason for choosing this test is that it is nonparametric and has no requirement on the distribution (Fay and Proschan 2010; Ma et al. 2015). Before applying this test, we first calculate the decorrelation time scales of the analyzed variables. Take the zonal wind at 850 hPa (U850) as an example: the decorrelation time scale is about 24 h. The daily mean field should give independently sampled time series. Then the distribution for each of the experiments (CTRL and MEFS) is computed based on the daily mean data from all 10 ensemble members at each grid point. Finally, median values of the two distributions are tested to see if they are significantly different (Ma et al. 2015). Not all the points that pass a significance test are shown in the figures, as we skip every 6 (2) data points when plotting HR (LR) simulation results for clarity purposes. To test the robustness of the results, we also repeat the statistical test using 3-day-averaged time series or dividing the ensemble into two randomly selected five-member ensembles; the test results show little change.

3. Model validation

Before proceeding to the examination of the effect of mesoscale SSTs on the atmosphere, we first evaluate the fidelity of WRF simulations by comparing model results against observations.

a. Winter mean rainfall and mean flow

The performance of WRF in simulating the winter mean rainfall and atmospheric circulation is validated

by comparing model results against observations and reanalysis data during the winter of 2007/08. The rainfall data used are the daily Tropical Rainfall Measuring Mission rainfall (TRMM 3B42) with 0.25° horizontal resolution. These satellite rainfall measurements are available within the latitude belt between 45°S and 45°N. Winds derived from 6-hourly European Centre for Medium-Range Weather Forecasts (ECMWF) interim reanalysis (ERA-Interim) data (Dee et al. 2011) are used to validate simulated mean flow.

Validation analyses are performed using the last five months [November–March (NDJFM)] of the WRF simulations with the first month of the simulations (October of 2007) considered as model spinup (Skamarock 2004). Figure 2 (left) shows a comparison of 2007/08 winter season (NDJFM) mean rainfall simulated in HR-CTRL and LR-CTRL, and in TRMM during the same period. In the observation, a high rainfall band collocates with the Kuroshio path in the northwestern Pacific (Fig. 2a) and is associated with a strong surface convergence along the front (Minobe et al. 2008). The model reproduces well the overall pattern and the position of the high rainfall band in both HR-CTRL and LR-CTRL except that the rainfall rate is overestimated in the former (Fig. 2c) but underestimated in the latter (Fig. 2e). The overestimation (by ~20%) in HR-CTRL mainly occurs downstream of the Kuroshio Extension and is likely attributable to the Kain–Fritsch convection scheme used in the model (Patricola et al. 2012, 2016). The underestimation (by ~40%) in LR-CTRL is an indication of insufficient horizontal resolution that cannot resolve intense precipitation events associated with midlatitude fronts and cyclogenesis.

Figure 2 (right) shows a comparison of 850- (color) and 300-hPa (contours) winter mean zonal wind U derived from ERA-Interim (Fig. 2b) and from HR-CTRL (Fig. 2d) and LR-CTRL (Fig. 2f). In ERA-Interim, the 850-hPa jet is centered along 40°N in the western Pacific, reaches maxima downstream of the Kuroshio, and tilts northeastward as it extends further into the eastern North Pacific basin. The upper-level jet stream is centered along 35°N in the western Pacific, with the maxima located along the Kuroshio. Both the high- and low-resolution WRF simulate well the overall structure of the jet stream, including its position and amplitude, except that the low-level jet is a bit too strong and the position shifted slightly northward.

b. Winter mean storm track

The midlatitude climate system is dominated by synoptic storms during winter. We use the meridional wind component derived from 6-hourly ERA-Interim data to validate the simulated North Pacific storm track. A

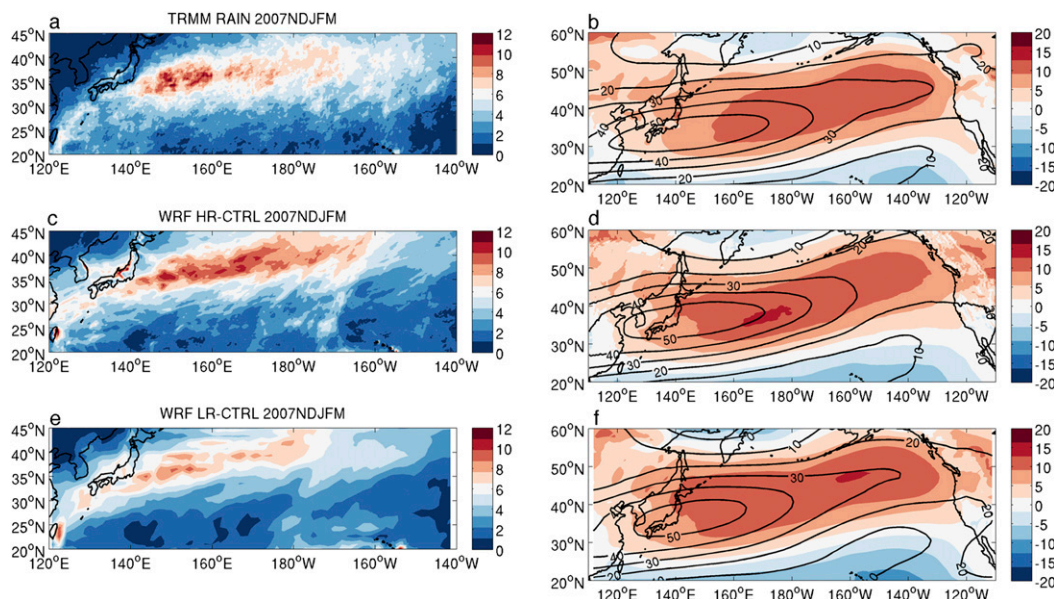


FIG. 2. The 2007/08 winter season (NDJFM) mean rainfall (mm day^{-1}) derived from (a) TRMM 3B42 and from (c) HR-CTRL and (e) LR-CTRL. (b),(d),(f) As in (a),(c),(e), but for the mean U850 (m s^{-1} ; color shaded) and U300 (m s^{-1} ; contours).

comparison of the lower- and upper-level storm tracks between ERA-Interim and the WRF simulations is illustrated in Fig. 3. The storm track is represented using the variance of 2–8-day bandpass-filtered meridional wind. The maximum of the 850-hPa storm track extends northeastward from 160°E to 140°W , downstream and north of the KER (Fig. 3a). The strong baroclinic instability induced by the sharp temperature gradient along the Kuroshio Front is responsible for the generation of the storm track, and upon its generation the storm track tends to follow a southwest–northeast path (Chang et al. 2002; Nakamura et al. 2008). The storm track at 300 hPa, which is much stronger, develops farther downstream and reaches a maximum over the eastern North Pacific and North American continent (Fig. 3b). The simulated storm track at 850 and 300 hPa in HR-CTRL (Figs. 3c,d) displays similar spatial patterns and axis of maxima as in ERA-Interim. However, storm-track strength in HR-CTRL is slightly stronger than that in the reanalysis possibly owing to the physics parameterizations and the higher spatial resolution used in the WRF simulations. In contrast, the storm track in LR-CTRL is much too weak at 850 hPa, and the path is distorted in comparison to ERA-Interim (Fig. 3e). At 300 hPa, its strength is also somewhat underestimated in LR-CTRL (Fig. 3f).

c. Planetary boundary response to mesoscale SST

A defining feature of the mesoscale air–sea interaction along the KER is that mesoscale high (low)

wind speed tends to collocate with warm (cold) mesoscale SST (Chelton et al. 2004). In HR-CTRL, not only is the observed covariability of mesoscale SST and surface wind well reproduced, but also the amplitude of high and low wind speeds simulated by the model agree very well with the observations, as shown in Ma et al. (2015). Ma et al. (2015) further show the covariability of mesoscale SST and PBL height anomalies along the KER, consistent with previous studies (Chelton et al. 2004; O'Neill et al. 2005; Small et al. 2008), and a coherent deep upper-troposphere response as indicated by the convective available potential energy (CAPE), as well as a mesoscale-SST-induced rainfall response that is consistent with the study by Frenger et al. (2013). These results demonstrate that the high-resolution WRF can faithfully capture mesoscale air–sea interactions along the KER and reproduce the observed local atmospheric boundary layer response to mesoscale SSTs induced by oceanic eddies. In the following, we focus on the comparison between HR-CTRL and LR-CTRL in simulating the covariability between mesoscale SST and surface turbulent heat fluxes (THFs) because SST–THF covariability is an important measure of mesoscale air–sea interactions in the region.

To estimate mesoscale SST–THF relationship in observations, we first apply the Loess filter to SST and THF derived from the National Centers for Environmental Prediction (NCEP) Climate Forecast System Reanalysis (CFSR; Saha et al. 2010) to extract mesoscale SST and THF variability, respectively, and then examine their

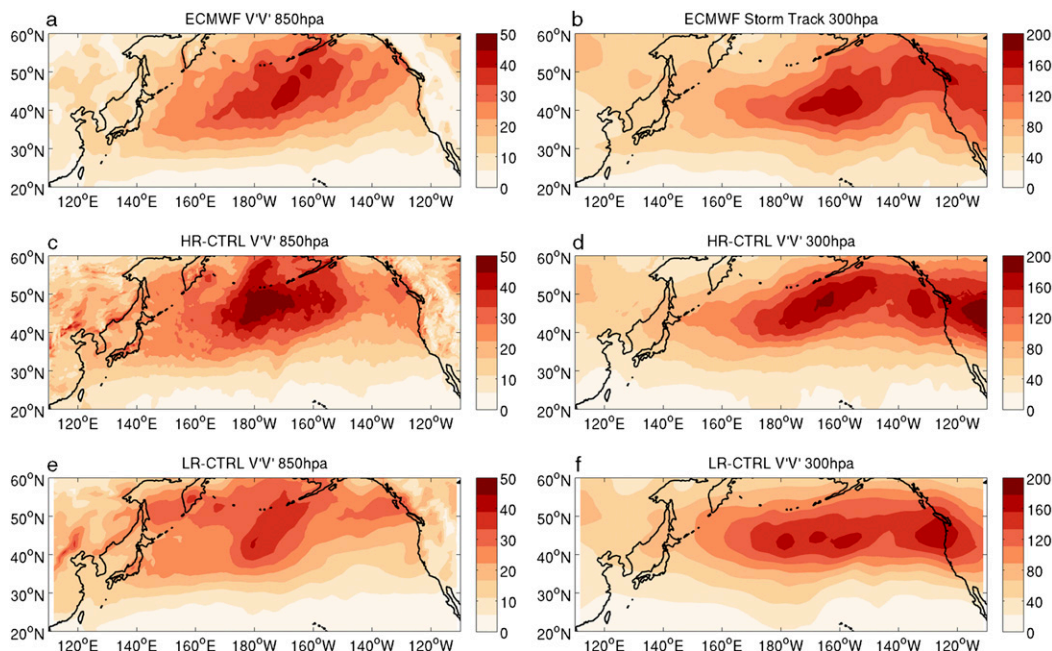


FIG. 3. The 2007/08 winter season (NDJFM) storm track at (left) 850 and (right) 300 hPa derived from (a),(b) ERA-Interim and from (c),(d) HR-CTRL and (e),(f) LR-CTRL. The storm track is defined using the standard deviation of the 2–8-day bandpass-filtered meridional wind component.

covariability. Figure 4a shows winter mean mesoscale THF overlaid on mesoscale SST in the KER from NCEP CFSR. There is a clear high-level coherence between mesoscale SST and THF with warm (cold) SST anomalies corresponding to positive (negative) THF out of the ocean, indicating that the ocean is releasing thermal energy to the atmosphere at mesoscales. Similar analyses performed for HR-CTRL and LR-CTRL show similar spatial coherence between mesoscale SST and THF (Figs. 4b,c). However, the amplitudes of the mesoscale SST and THF show a clear resolution dependence. In HR-CTRL, the winter mean mesoscale SSTs are comparable in strength to those in NCEP CFSR by design, but the corresponding surface THFs tend to be stronger than NCEP CFSR. This may be related to the fact that HR-CTRL is conducted at a finer resolution (27 km) than NCEP CFSR at T382 ($\sim 0.325^\circ$). In LR-CTRL, both the mesoscale SSTs and THFs are considerably weaker because of the coarse resolution (162 km) that cannot fully resolve mesoscale oceanic eddies.

To further quantify the mesoscale SST–THF relationship, we show density plots of weekly averaged mesoscale SST and THF for 2007/08 winter in Figs. 4d–f. As can be seen, mesoscale SST and THF anomalies are highly correlated in both the NCEP CFSR and WRF simulations. Linear regression coefficients between mesoscale SST and THF anomalies can be used as a

measure of “thermal coupling strength” between oceanic mesoscale eddies and atmosphere in the KER. In NCEP CFSR, the thermal coupling strength is estimated at $\sim 46 \text{ W}^\circ\text{C}^{-1}$ that is below the value of $54 \text{ W}^\circ\text{C}^{-1}$ for HR-CTRL, but slightly above the value of $44 \text{ W}^\circ\text{C}^{-1}$ for LR-CTRL. It is worth pointing out that the thermal coupling strengths obtained in this study using the high-resolution data are comparable to previous estimates in the region based on coarse-resolution SST and THF datasets (Frankignoul et al. 2002; Park et al. 2005). Interestingly, the coupling coefficient does not show strong sensitivity to mesoscale SST forcing strength. When the mesoscale SST forcing strength is amplified by a factor of 1.5 in M-LR-CTRL, the coupling coefficient remains essentially the same as the value in LR-CTRL as shown by the red line in Fig. 4f. This result suggests that the $\sim 20\%$ reduction in the thermal coupling strength in the low-resolution WRF simulations compared to the high-resolution simulation is caused not by the reduced mesoscale SST variance but by the insufficient spatial resolution to properly resolve ocean mesoscale eddy–atmosphere interactions over the KER.

In summary, the high-resolution WRF demonstrates high fidelity in simulating rainfall, jet stream, and storm tracks over the North Pacific. It also demonstrates a remarkable skill in reproducing observed mesoscale SST–THF relationships over the KER, indicating its capability of capturing frontal- and mesoscale air–sea

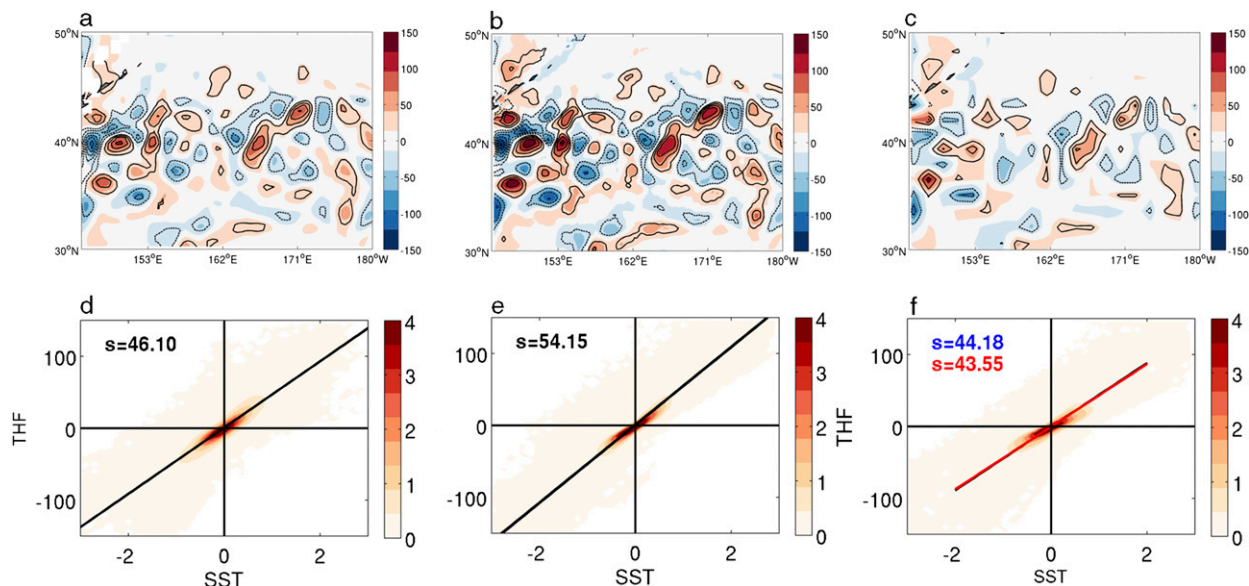


FIG. 4. The 2007/08 winter season mean (NDJFM) spatially high-pass-filtered SST (contours; $^{\circ}\text{C}$) and THF (color shaded; W m^{-2}) derived from (a) NCEP CFSR and from (b) HR-CTRL and (c) LR-CTRL. (d),(e),(f) As in (a),(b),(c), but for a density plot (number of points in K) and linear regression (black lines) based on weekly high-pass-filtered SST and THF. Red line in (f) indicates the linear regression between weekly high-pass-filtered SST and THF for M-LR-CTRL.

coupled dynamics in the region. In comparison, the overall patterns of rainfall, jet stream, and storm track are also captured in the low-resolution WRF simulations, except that the response exhibits more biases compared to the high-resolution WRF simulations. In particular, the simulated rainfall and lower-level storm track appear to be underestimated. These biases are likely attributable to the fact that the coarse-resolution model cannot properly resolve moist diabatic processes that are critically important for extratropical cyclogenesis as hypothesized by Willison et al. (2013) and Ma et al. (2015). This hypothesis will be further tested in section 5.

4. Impact of mesoscale SSTs on storm track and large-scale atmospheric circulation

Having established the high fidelity of WRF in simulating local atmospheric PBL responses to mesoscale SSTs along the KER, we now examine the potential impact of these mesoscale SSTs on the Pacific storm track and large-scale atmospheric circulation. In particular, we will investigate the resolution dependence of the modeled storm track and large-scale circulation response to mesoscale SST forcing by comparing high-resolution WRF simulations to low-resolution simulations.

The KER is known as an important region for mid-latitude cyclogenesis in the North Pacific, raising the

possibility that mesoscale oceanic eddies in this region may have an impact on storm systems. To explore this possibility, we examined and compared lower- and upper-level storm-track changes in WRF simulations. Figures 5a,c (Figs. 5b,d) show the difference of winter season mean meridional transient eddy heat transport $\langle v'T' \rangle$ at 850 hPa and variance of the v' wind $\langle v'v' \rangle$ at 300 hPa between HR-MEFS and HR-CTRL (LR-MEFS and LR-CTRL), respectively. Here, the prime represents 2–8-day bandpass-filtered data. For the high-resolution simulations, removal of mesoscale oceanic eddies results in a significant decrease ($\sim 15\%$) in eddy heat transport at 850 hPa along the KER from 140°E to 160°W (Fig. 5a), indicating weakened cyclogenesis in this region. In the eastern North Pacific, there is an increase of $\langle v'T' \rangle$ in the south and a decrease in the north, suggesting a southward shift of the downstream storm track at this level (Fig. 5a). At the upper level (300 hPa), the decrease of storm activity along the KER becomes less evident while the downstream southward shift of the storm track becomes a more dominant pattern, particularly east of 140°W (Fig. 5c). This change in the lower- and upper-level storm track between HR-MEFS and HR-CTRL demonstrates that removal of mesoscale SST variability can not only influence the local cyclogenesis but also have a remote effect on the downstream development of storms. In the low-resolution simulations, the changes in eddy activity are much smaller and less significant at both the lower and upper level (Figs. 5b,d).

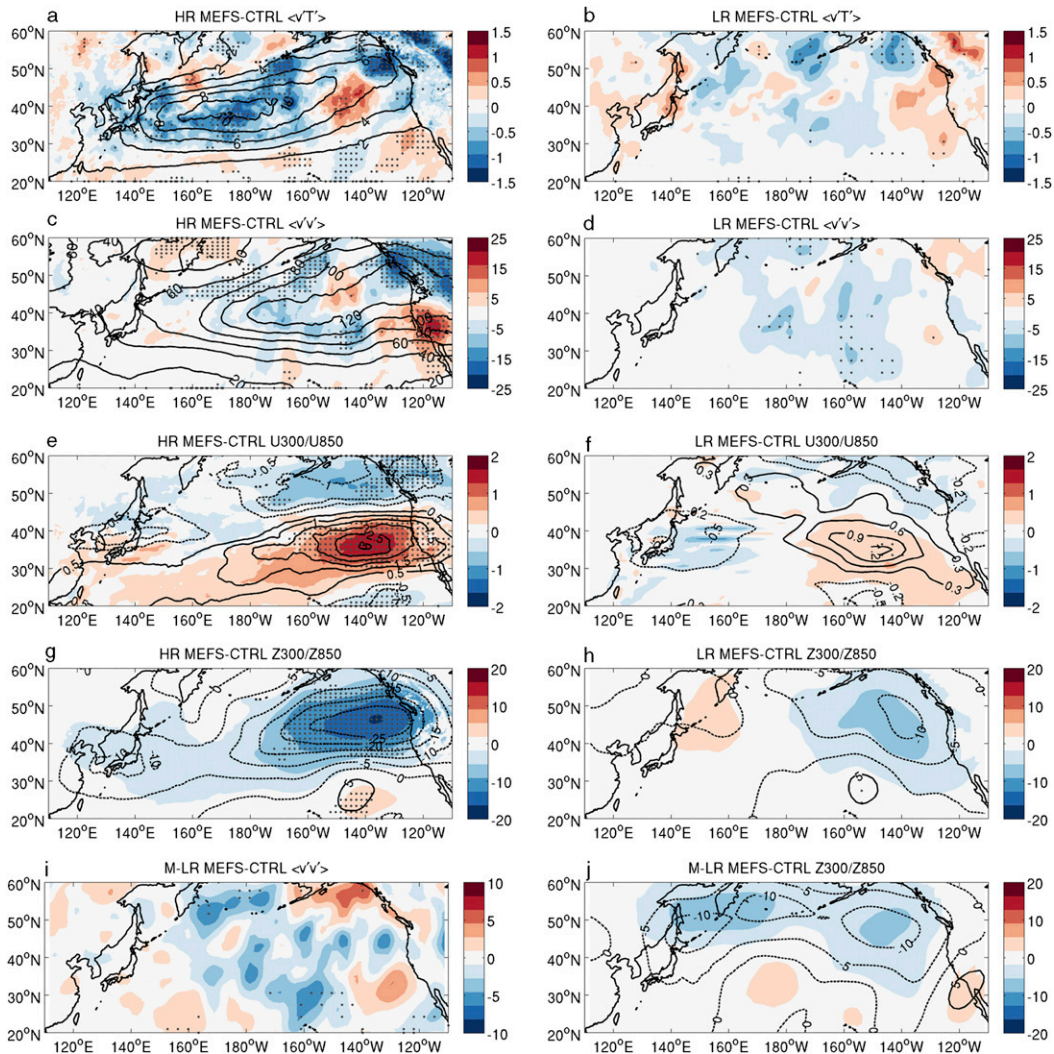


FIG. 5. Winter season mean (a) transient eddy heat transport $\langle v'T' \rangle$ at 850 hPa (contours; $\text{m s}^{-1} \text{K}$) and (c) storm-track $\langle v'v' \rangle$ at 300 hPa (contours; $\text{m}^2 \text{s}^{-2}$) simulated in HR-CTRL. Difference of winter season mean (a) transient eddy heat transport $\langle v'T' \rangle$ at 850 hPa (color shaded; $\text{m s}^{-1} \text{K}$), (c) storm-track $\langle v'v' \rangle$ at 300 hPa (color shaded; $\text{m}^2 \text{s}^{-2}$), (e) zonal wind at 850 hPa (U850; color shaded; m s^{-1}) and at 300 hPa (U300; contours; m s^{-1}), and (g) geopotential height at 850 hPa (Z850; color shaded; m) and at 300 hPa (Z300; contours; m) differences between HR-MEFS and HR-CTRL. (b),(d),(f),(h) As in (a),(c),(e),(g), but for differences between LR-MEFS and LR-CTRL. Difference of winter season mean (i) storm-track $\langle v'v' \rangle$ at 300 hPa (color shaded; $\text{m}^2 \text{s}^{-2}$) and (j) Z850 (color shaded; m) and Z300 (contours; m) differences between LR-MEFS and M-LR-CTRL. The difference, significant at the 95% confidence level based on a two-sided Wilcoxon rank sum test, is shaded by dots. See Ma et al. (2015) for details of the significance test.

In particular, there is no marked decrease in 850-hPa $\langle v'T' \rangle$ along the KER, nor is there a significant southward shift in 300-hPa $\langle v'v' \rangle$ in the eastern North Pacific.

The muted atmospheric response to mesoscale SST forcing in the low-resolution simulations is also reflected by changes in large-scale atmospheric circulation between the twin ensembles. Figures 5e,g (Figs. 5f,h) show the difference of winter season mean of lower-level (850 hPa) and upper-level (300 hPa) jet stream and GPH in the North Pacific between HR-MEFS and HR-CTRL

(LR-MEFS and LR-CTRL), respectively. In the high-resolution ensembles, removing mesoscale SST forcing results in a significant southward displacement of both the lower- and upper-level jet stream in the eastern North Pacific (Fig. 5e), consistent with the southward shift of storm-track response (Fig. 5c). Correspondingly, the lower- and upper-level winter mean GPH display a negative anomaly to the east of the center of the Aleutian low, consistent with the mean flow change in the eastern North Pacific (Fig. 5g). Together, these changes

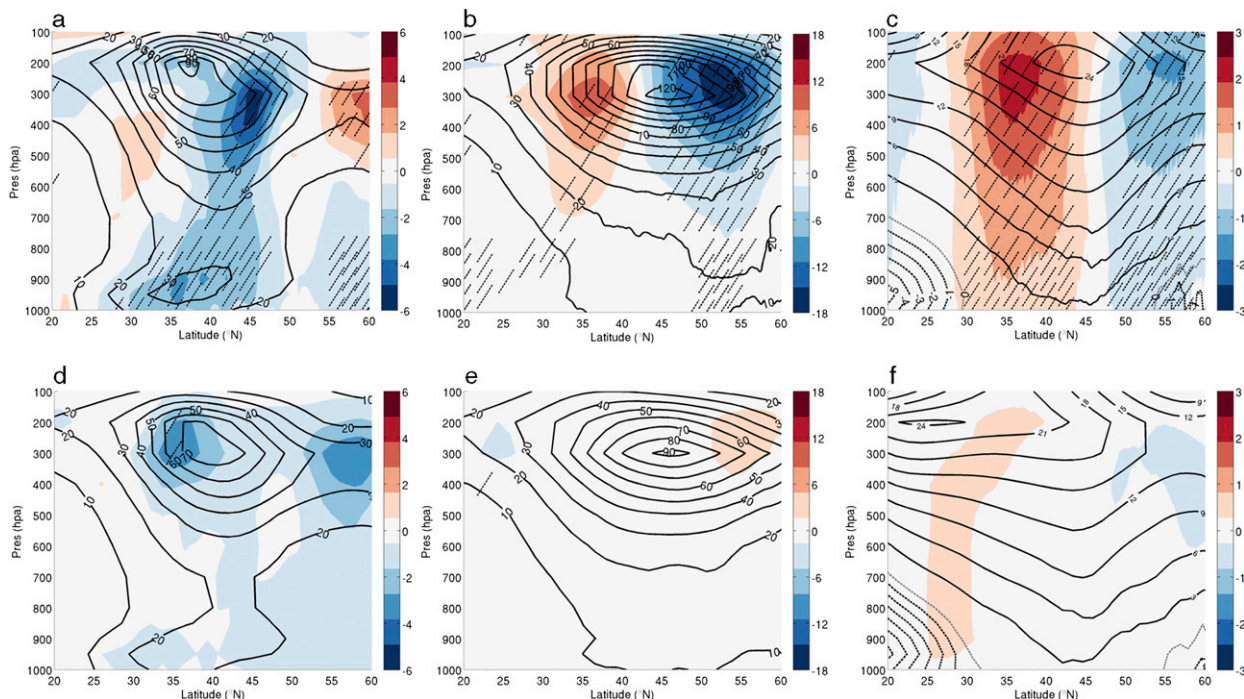


FIG. 6. (a) Vertical profile of winter season mean (contours) storm-track $\langle v'v' \rangle$ in the KER averaged from 150°E to 180° and simulated in HR-CTRL and difference (color shaded) of that between HR-MEFS and HR-CTRL ($\text{m}^2 \text{s}^{-2}$). (b),(c) As in (a), but for (b) storm-track $\langle v'v' \rangle$ ($\text{m}^2 \text{s}^{-2}$) and (c) zonal wind U (m s^{-1}) in the eastern North Pacific averaged from 140° to 110°W . (d)–(f) As in (a)–(c), but for low-resolution simulations. The difference significant at the 95% confidence level based on a two-sided Wilcoxon rank sum test is marked by hatching.

in the mean flow and GPH depict an equivalent barotropic response of the atmosphere circulation in the eastern North Pacific in response to the mesoscale SST forcing largely confined in the KER. In contrast, the atmospheric responses in the low-resolution ensembles are mostly insignificant, with only a few small areas of change in mean zonal winds and GPH between LR-CTRL and LR-MEFS passing the significance test (Figs. 5f,h). We also note that when the mesoscale SST forcing is amplified by 50% in M-LR-CTRL, there is still no significant storm-track and mean flow change (Figs. 5i,j), indicating that this lack of significant response in the low-resolution ensembles is not simply caused by the reduced amplitude of mesoscale SST forcing variance in the low-resolution simulations.

The different storm-track and mean flow responses to mesoscale SST forcing between the high- and low-resolution ensembles can be seen more clearly in the vertical cross section (Fig. 6). Figure 6a shows the zonally averaged $\langle v'v' \rangle$ in the KER (150°E – 180°) in the HR-CTRL (contour). The model clearly captures the northward tilt of transient eddy variance with increasing height as in observations (Booth et al. 2010). The difference of $\langle v'v' \rangle$ between HR-MEFS and HR-CTRL (Fig. 6a, color) shows that there is a local decrease of the storm activity from the surface to the upper troposphere

in the KER. Figure 6b shows a similar plot of the vertical structure in the far-eastern North Pacific (140° – 110°W), which reveals a clear dipole response in storm-track change with an increase ($\sim 20\%$) of $\langle v'v' \rangle$ between 30° and 40°N and decrease ($\sim 20\%$) between 50° and 60°N . The downstream storm-track change also is mainly confined within the upper troposphere with little change below 700 hPa, suggesting that it is unlikely that the change originated from local SST forcing in the eastern North Pacific. A similar dipole response in the mean zonal winds is found in the far-eastern North Pacific (Fig. 6c), and the resultant vertical structure is consistent with an equivalent barotropic response with decreasing response amplitude toward the surface.

Similar vertical section plots for the low-resolution simulations are shown in Figs. 6d–f. In the KER, although there is still a decrease of $\langle v'v' \rangle$ from the surface to the upper troposphere in response to the removal of the mesoscale SST forcing, the response is weak and does not pass the significance test at the 95% level, and there is a lack of the northward tilt in the response with height as expected from baroclinic transient eddies (Fig. 6d). In the eastern North Pacific, the response is even weaker with an opposite sign to that in the high-resolution ensembles (Fig. 6e). Correspondingly, the equivalent barotropic response in the eastern North

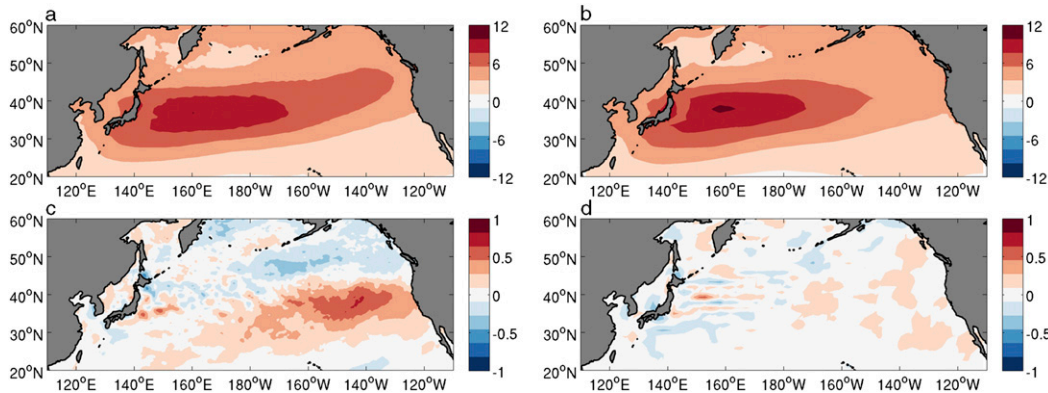


FIG. 7. Winter season mean Eady growth rate (10^{-1} day^{-1}) at 850 hPa computed from (a) HR-CTRL and (b) LR-CTRL. Difference of this growth rate (c) between HR-MEFS and HR-CTRL and (d) between LR-MEFS and LR-CTRL.

Pacific also disappears in the low-resolution simulations (Fig. 6f). Moreover, the vertical structure of the jet stream simulated in LR-CTRL (contours in Fig. 6f) is distorted with the jet core displaced southward to near 25°N . Together, these results indicate that insufficient resolution can lead to unrealistic simulation of the storm track and large-scale atmospheric response to mesoscale SSTs.

In summary, high-resolution WRF simulations show that mesoscale SST forcing can exert a statistically significant impact on the North Pacific storm track and atmospheric circulation. When mesoscale SST forcing is suppressed, the model simulations reveal a reduced ($\sim 15\%$) eddy heat transport in the KER and an intensified ($\sim 20\%$) cyclonic low pressure accompanied by a southward shift of the storm track and jet stream in the eastern North Pacific. In contrast, such statistically significant differences between low-resolution twin ensembles are not found. This is the case even when the mesoscale SST forcing is amplified by 50% in M-LR-CTRL, indicating that the lack of robust responses in the low-resolution simulations is not simply related to the strength of the SST forcing.

5. Dynamics of mesoscale-SST-forced atmospheric response

This section is devoted to the understanding of the dynamics responsible for the local and remote atmospheric response to mesoscale SST forcing and of the importance of adequate model resolution. We address these issues by carrying out a set of diagnostic analyses.

a. Diagnostic of atmospheric baroclinicity

We begin our analyses by first examining whether the mesoscale SST forcing can alter atmospheric baroclinicity in the KER that, in turn, can affect cyclogenesis.

Many previous studies have linked changes of midlatitude storm track to changes in atmospheric baroclinicity caused by changes in underlying SST gradients (Nakamura et al. 2008; Joyce et al. 2009). According to the classic baroclinic theory, lower-level baroclinic instability can be effectively measured by the Eady growth rate, which depends on the ratio between vertical wind shear and Brunt–Väisälä frequency (Hoskins and Valdes 1990). Ma et al. (2015) computed the Eady growth rate for HR-CTRL and HR-MEFS and found little change between HR-CTRL and HR-MEFS over the KER. Figure 7 compares the Eady growth rate and its change at 850 hPa between the high- and low-resolution simulations. Consistent with the theory, the maximum of the Eady growth rate in both HR-CTRL and LR-CTRL is located along the KER where the underlying SST gradient is strongest (Figs. 7a,b). Interestingly, the Eady growth rate is slightly stronger in the low-resolution simulations than in the high-resolution simulations, in spite of the weaker transient eddy variance in the former. It suggests that resolution does not have a major influence on dry baroclinic instability. It also implies that dry baroclinic instability is not the only factor determining transient eddy activity. This assertion is further reinforced by the changes of Eady growth rate shown in Figs. 7c,d; removal of mesoscale SST forcing leads to little change in Eady growth rate ($<1\%$) in the KER. Therefore, it is unlikely that the difference in cyclogenesis and storm track between HR-CTRL and HR-MEFS can be simply explained by the classic baroclinic instability theory. This is consistent with the notion that the influence of oceanic eddies, which have spatial scales much smaller than the atmospheric Rossby radius, averages out to zero in dry baroclinic instability theory, provided the mean flow changes over the KER region are small between HR-CTRL and HR-MEFS. We note that in the high-resolution

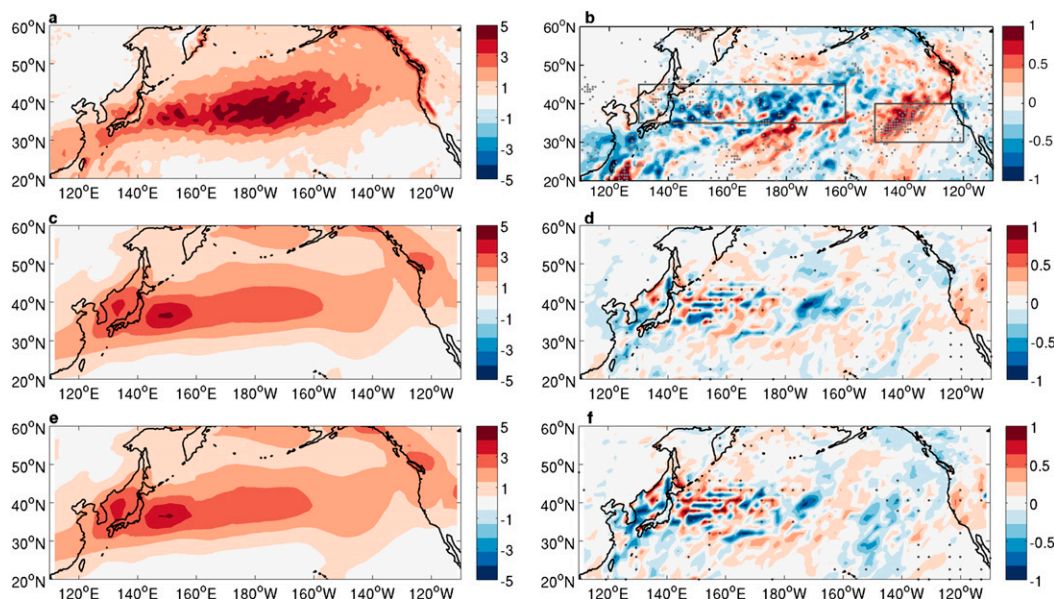


FIG. 8. Vertically integrated (from 1000 to 300 hPa) diabatic heating (Pa K s^{-1}) averaged over storm days in (a) HR-CTRL, (c) LR-CTRL, and (e) M-LR-CTRL. The diabatic heating difference between (b) HR-MEFS and HR-CTRL, (d) LR-MEFS and LR-CTRL, and (f) LR-MEFS and M-LR-CTRL. Because of the noisy structure of diabatic heating difference, an additional significance test was performed on area-averaged differences in two chosen regions $[(35^{\circ}\text{--}45^{\circ}\text{N}, 130^{\circ}\text{E--}160^{\circ}\text{W})$ and $(30^{\circ}\text{--}40^{\circ}\text{N}, 150^{\circ}\text{--}120^{\circ}\text{W})]$ as indicated by the two boxes in (b), where atmospheric response is the strongest. The resultant test results show that these area-averaged differences are significant at the 95% confidence level based on a two-sided Wilcoxon rank sum test for the high-resolution ensemble in (b) but not for the low-resolution ensembles in (d),(f).

simulations, there is a marked southward shift of the Eady growth rate in the eastern North Pacific (Fig. 7c), which is likely to be associated with the jet stream change in the region (e.g. Fig. 6c).

b. Diagnostic of moist diabatic effect

As suggested by Ma et al. (2015), a likely candidate for linking mesoscale SST forcing to storm-track response is moist baroclinic instability. According to moist baroclinic instability theory, the presence of diabatic heating release in a moist atmosphere can significantly reduce the static stability, enhance vertical mixing, and lead to stronger baroclinic growth rate (Ahmadi-Givi et al. 2004; Davis and Emanuel 1991; Emanuel et al. 1987). To examine this possibility, we focus on cyclogenesis periods in the simulations and examine how moist diabatic processes affect cyclogenesis with and without mesoscale SST forcing. To define “storm days,” we use a THF threshold criterion, in which first we select all periods during which the daily mean THF averaged over the KER ($32^{\circ}\text{--}42^{\circ}\text{N}$, $140^{\circ}\text{--}170^{\circ}\text{E}$) exceeds its 80th percentile and then for each of these periods we choose the day corresponding to the maximum THF as a storm day. Physically, this selection identifies the days when strong cyclones occur slightly downstream of the KER, leading to extreme THF values in the region (see Ma et al. 2015

for details). The resultant storm days in each ensemble account for about 20% of total winter season days from November to March. Figures 8a,b show the storm-day diabatic heating simulated in HR-CTRL and the difference of storm-day diabatic heating between HR-MEFS and HR-CTRL. In HR-CTRL, intensified diabatic heating with marked mesoscale structures occurs along the KER. The maximum diabatic heating is located slightly downstream of the KER, following the initial cyclone growth (Fig. 8a). In HR-MEFS, there is an overall decrease ($\sim 20\%$) of diabatic heating release centered along the Kuroshio path (Fig. 8b). In contrast, diabatic heating in LR-CTRL is considerably weaker compared to HR-CTRL with no visible mesoscale structures along the KER (Fig. 8c). The result suggests that at 27 km WRF is able to better resolve small-scale ageostrophic vertical motions during cyclogenesis that lead to the stronger and narrower frontal-scale diabatic heating structures, as shown in previous studies (Orlanski 2008; Willison et al. 2013). Weak diabatic heating with similar structure to that in LR-CTRL also occurs in M-LR-CTRL even when mesoscale SSTs are amplified by 50% (Fig. 8e), further indicating the importance of resolving small-scale ageostrophic vertical motions that influence mesoscale diabatic heating rather than just the strength of the mesoscale SST forcing. We note that owing to the noisy

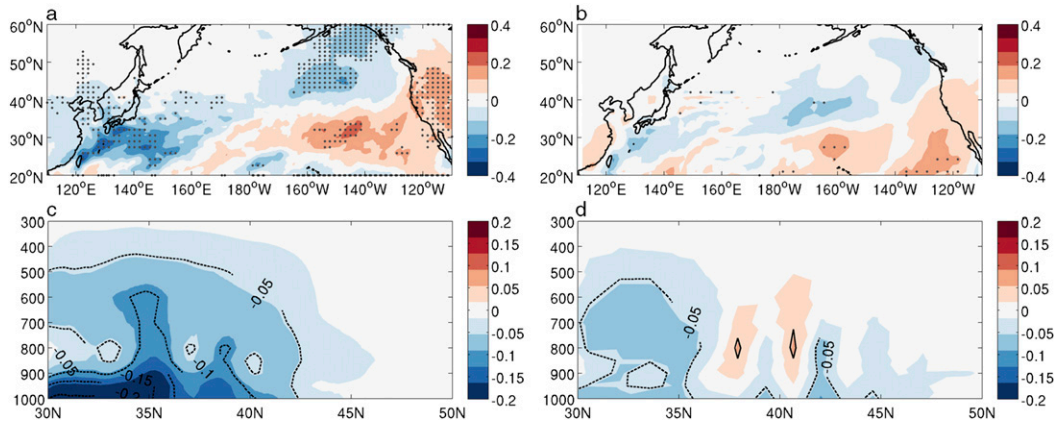


FIG. 9. Difference of vertically integrated (from 1000 to 300 hPa) water vapor mixing ratio Q_v ($\text{kg m}^{-1} \text{s}^{-2}$) averaged over storm days (a) between HR-MEFS and HR-CTRL and (b) between LR-MEFS and LR-CTRL. Vertical section of zonally averaged (from 140°E to 180°) Q_v difference (c) between HR-MEFS and HR-CTRL and (d) between LR-MEFS and LR-CTRL. Positive (negative) values are contoured in solid (dashed) in (c),(d). The difference significant at the 95% confidence level based on a two-sided Wilcoxon rank sum test is shaded by dots in (a),(b).

nature of the frontal-scale diabatic heating, the statistical significant test performed on diabatic heating differences results in noisy patterns in Figs. 8b,d,f. To ensure the credibility of the significant test results, we performed a “field significance” test by using area-averaged values over regions where atmospheric response is the strongest as indicated by two boxes in Fig. 8b. As expected, the resultant area-averaged diabatic heating differences in these two regions are both statistically significant at the 95% confidence level in the high-resolution ensembles (Fig. 8b) but not in the low-resolution ensembles (Figs. 8e,f).

The above finding is consistent with Willison et al. (2013), who showed the narrowness of diabatic heating bands associated with intensified precipitation during cyclogenesis and emphasized the importance of accurately representing the narrow diabatic heating in simulating cyclogenesis. They suggested a horizontal resolution of ~ 20 km is necessary to adequately represent the diabatic heating. This resolution requirement is marginally satisfied by our 27-km high-resolution model but certainly not met by the 162-km low-resolution model. Thus, even when mesoscale SST forcing is suppressed in LR-MEFS, no obvious changes in diabatic heating in the KER are found, as shown in Figs. 8d,f, consistent with the lack of a robust storm track and mean flow responses in the low-resolution simulations as shown in Fig. 5.

Figures 9a,b show the difference of storm-day water vapor mixing ratio between HR-MEFS and HR-CTRL and between LR-MEFS and LR-CTRL, respectively. During storm days, removal of mesoscale SST forcing in HR-MEFS leads to an overall decrease (30%–40%) of water vapor mixing ratio Q_v in the KER and an increase

of Q_v in the eastern North Pacific (Fig. 9a), compared to a $\sim 10\%$ change of winter season mean Q_v between MEFS and CTRL (figure not shown). A close look at the vertical section of the Q_v reduction in the KER (Fig. 9c) reveals that the maximum moisture change is confined within the PBL with some changes in the lower troposphere below 500 hPa. The reductions in storm-day averaged Q_v and diabatic heating along the KER point to a rectified effect of mesoscale oceanic eddies on the atmosphere, which partly arises from the nonlinearity in the Clausius–Clapeyron saturation vapor pressure relationship that gives a disproportionately larger impact on boundary layer humidity from warm ocean eddies than cold eddies (Deser et al. 2004; Ma et al. 2015). In line with the diabatic heating analysis results, the decrease in Q_v is considerably smaller and does not pass the significance test in LR-MEFS (Figs. 9b,d).

Unlike a dry atmosphere in which baroclinic transient eddy potential energy (EPE) gain is derived from mean available potential energy (MAPE), in a moist atmosphere EPE gain can be derived from both MAPE and diabatic sources. Figures 10a–c show the difference of storm-day diabatic conversion $\langle T' \partial Q' / \partial z \rangle$ between the twin ensembles at various model resolutions. Here Q represents the diabatic heating, the prime is defined as perturbations from climatological monthly mean using all 10 ensemble members, and the brackets stand for the time average for all the storm days in all 10 ensemble members. Consistent with the moist baroclinic instability, removal of the mesoscale SSTs significantly reduces the diabatic conversion in the high-resolution ensembles (Fig. 10a). During cyclogenesis, EPE gain is converted to eddy kinetic energy (EKE) that determines

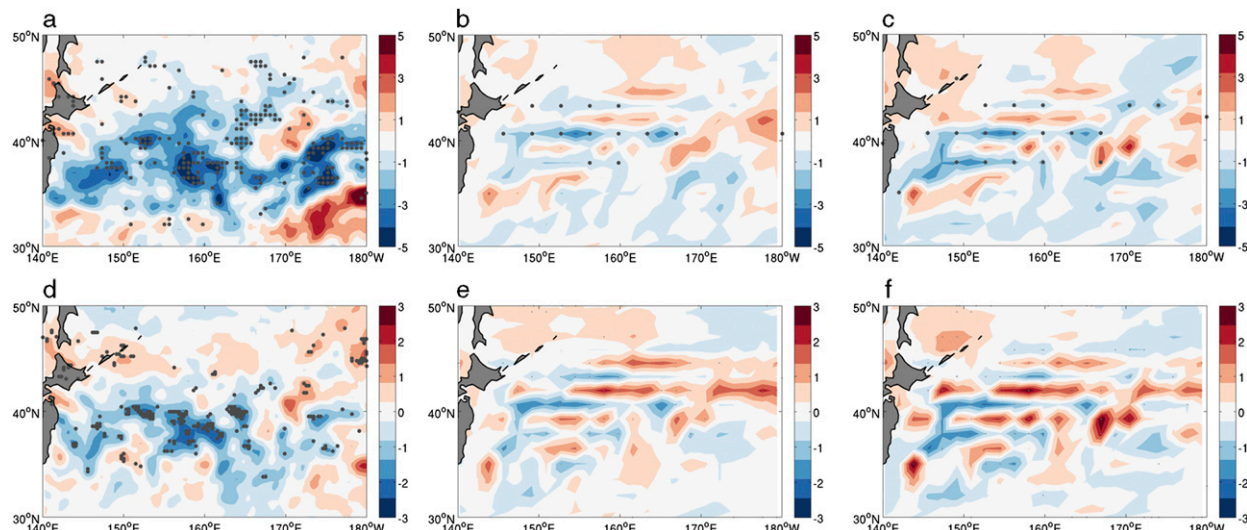


FIG. 10. Difference of vertically integrated (from 1000 to 300 hPa) diabatic conversion $\langle T' \partial Q' / \partial z \rangle$ ($\text{Pa K}^2 \text{s}^{-1}$) averaged over storm days in the KER (a) between HR-MEFS and HR-CTRL, (b) between LR-MEFS and LR-CTRL, and (c) between LR-MEFS and M-LR-CTRL. (d)–(f) As in (a)–(c), but for difference of vertically integrated $\langle w' T' \rangle$ ($10^{-2} \text{ m s}^{-1} \text{ K}$). The difference significant at 95% confidence level based on a two-sided Wilcoxon rank sum test is shaded by dots.

overall storm intensity. Since there is substantial change of diabatic conversion, one expects EPE-to-EKE conversion to differ significantly between the simulations with and without mesoscale SST forcing. We estimate EPE-to-EKE conversion by computing $\langle w' T' \rangle$ (Figs. 10d–f). Consistent with the diabatic conversion analysis, in the high-resolution ensembles there is a significant decrease in EPE-to-EKE conversion when mesoscale SSTs are suppressed in HR-MEFS (Fig. 10d). In contrast, for the low-resolution ensembles, changes of both diabatic and EPE-to-EKE conversion are patchy and mostly insignificant for both LR-CTRL versus LR-MEFS and M-LR-CTRL versus LR-MEFS (Figs. 10b,c,e,f), further confirming that it is the accuracy of representing narrow diabatic heating rather than the amplitude of mesoscale SST forcing that contributes to the different storm-track response between the high- and low-resolution simulations.

In summary, diagnostics of moist diabatic processes are supportive of moist baroclinic instability being the prime linkage between mesoscale SST forcing and the storm-track response. In the high-resolution ensemble, removal of mesoscale SSTs results in a significant reduction in Q_v and diabatic heating as well as EPE-to-EKE conversion. Since atmospheric baroclinicity is not altered significantly by mesoscale SST forcing as shown in the previous subsection, one expects no significant changes in MAPE-to-EPE conversion. Therefore, the marked change in EPE-to-EKE conversion is mostly attributed to diabatic energy conversion. The results from the low-resolution simulations further back this claim. In contrast to the high-resolution ensembles, the low-resolution ensembles reveal neither

significant changes in cyclogenesis and storm-track response nor significant changes in atmospheric baroclinicity, diabatic heating, and EPE-to-EKE conversion. This is likely due to the fact that mesoscale SST-induced diabatic heating effect is not adequately resolved by the low-resolution model, causing insensitivity of atmospheric response to mesoscale SST forcing.

c. Diagnostic of transient eddy feedback

We next investigate dynamical processes that are responsible for the equivalent barotropic response in the eastern North Pacific to mesoscale SST forcing. Since this response is only revealed in the high-resolution simulations, we focus below on the comparison between HR-MEFS and HR-CTRL. It is well established that midlatitude atmospheric circulations are primarily driven by transient eddies (Hoskins et al. 1983; Held and Hoskins 1985). Thus, changes in transient eddy activity are likely responsible for the anomalous equivalent barotropic circulation developed in the eastern North Pacific via transient eddy feedback on the mean flow (Hoskins et al. 1983). To quantify this, we calculate the divergence of the \mathbf{E} vector that governs the feedback of transient eddies onto the mean flow (Hoskins et al. 1983). In the upper troposphere, the \mathbf{E} vector can be approximately expressed as follows (e.g., Hoskins et al. 1983):

$$\mathbf{E} = (\langle v'^2 - u'^2 \rangle, \langle -u'v' \rangle).$$

Here, v is the meridional and u the zonal wind; and the prime represents velocity induced by high-frequency

transient eddies defined by 2–8-day bandpass filtering. The angle bracket represents a time average. The horizontal divergence of the \mathbf{E} vector indicates an acceleration of mean flow caused by transient eddies and the convergence suggests a deceleration at a given level.

The divergence of the \mathbf{E} vector $\nabla \cdot \mathbf{E}$ contains pronounced small-scale features. To obtain the large-scale pattern of interests, it is necessary to apply a spatial average to the field (O'Reilly and Czaja 2015). Figures 11a,b show the spatially smoothed ($10^\circ \times 10^\circ$ boxcar filter) ensemble mean of $\nabla \cdot \mathbf{E}$ during NDJFM at 300 hPa in HR-CTRL and HR-MEFS, respectively. Clearly, transient eddies generate an \mathbf{E} -vector divergence downstream of the KER extending north-eastward from 150°E all the way to the eastern boundary of the Pacific Ocean (Fig. 11a). The location of the \mathbf{E} -vector divergence coincides with the jet core shown in Fig. 2, acting to accelerate the westerlies downstream of the Kuroshio Extension. In the HR-CTRL, the maximum divergence occurs in the western and central North Pacific, indicating that transient eddies travel a relatively short distance before dissipating and giving energy to the mean flow. The divergence in the HR-MEFS is generally weaker in the western and central North Pacific, clearly shown by the $\nabla \cdot \mathbf{E}$ difference between the two simulations (Fig. 11c), consistent with the reduced growth rate of storms in HR-MEFS. It is also worth noting that the most significant change in $\nabla \cdot \mathbf{E}$ occurs in the eastern North Pacific, suggesting that mesoscale SST forcing can not only modify cyclogenesis in the KER but also alter downstream storm development. We hypothesize that in the presence of mesoscale SST forcing (HR-CTRL), the strong baroclinic wave growth causes the waves to quickly saturate and enter barotropic decay phase, exerting eddy forcing on the mean flow in the central basin (Fig. 11a). In contrast, the waves in HR-MEFS develop more slowly, reaching their nonlinear saturation farther downstream and affecting the mean flow more effectively in the eastern North Pacific. When a zonal average of the difference of $\nabla \cdot \mathbf{E}$ is taken between 110° and 140°W , we observe a consistent southward shift of $\nabla \cdot \mathbf{E}$ that aligns with the mean flow change (not shown). This suggests that eddy–mean flow interaction may contribute to the southward shift of jet stream in the eastern North Pacific.

However, a close look at the $\nabla \cdot \mathbf{E}$ difference reveals a pattern dominated by a noisy component that does not clearly explain the equivalent barotropic circulation anomaly shown in Fig. 5. This noisy nature of $\nabla \cdot \mathbf{E}$ is also noted by O'Reilly and Czaja (2015) in their analysis of the atmospheric response to Kuroshio variability using observational and reanalysis data. In light of these results, we consider an alternative explanation: Can the

equivalent barotropic circulation anomaly be explained in terms of the accumulative effect of differing storm development between HR-CTRL and HR-MEFS? This will be the topic of the following section.

d. Accumulative storm effect on mean flow

As discussed above, mesoscale SST forcing can affect cyclogenesis through moist baroclinic instability, which in turn affects downstream storm development. Previous studies have shown that accumulative effects of winter storms can contribute to large-scale mean atmospheric circulation changes (Benedict et al. 2004; Feldstein 2003; Riviere and Orlanski 2007; Vallis and Gerber 2008). We examine this effect by tabulating all the simulated storm events during their life cycles and computing their accumulated difference between HR-CTRL and HR-MEFS. To identify storm events, we use an index based on the surface meridional wind V derived from HR-CTRL by taking an area average of V over the KER ($30^\circ\text{--}45^\circ\text{N}$, $140^\circ\text{--}160^\circ\text{E}$). We first find all the periods when negative V values (northerly winds) exceed the 80th-percentile threshold, and then define storm onset days as the days corresponding to the maximum negative V value within each of these periods. A life cycle of a storm event is defined as a period of 4 days that follows the storm onset day, during which the storm propagates from the KER to the eastern North Pacific (figure not shown). The total number of storm life cycle days accounts for less than half (approximately 47.5%) of the entire winter days (from November to March) and is referred to as the stormy period. The rest of the winter days are referred to as the less-stormy period. Stormy and less-stormy periods are identified based on HR-CTRL and made identical in HR-MEFS so that we can examine how the development of the storm systems in HR-CTRL is affected by the absence of mesoscale SST forcing in HR-MEFS. We note that the results shown below are not sensitive to the storm threshold value (using a 70th- or 75th-percentile threshold yields very similar results), and they are also not sensitive to the atmospheric variable used to define storm events. In fact, the results shown below are similar to those of Ma et al. (2015) where storm events were defined using a surface THF-based index.

Once stormy and less-stormy periods are identified in each ensemble, in both HR-CTRL and HR-MEFS we compute the sum of GPH at 850 and 300 hPa for each of these periods and divide by the total number of winter days. Note that the sum of the storm and less-stormy period composites computed in this manner is equal to the winter mean GPH. We then compute the difference of GPH composite between HR-MEFS and HR-CTRL in the storm and less-stormy period. Figures 12a,b display these

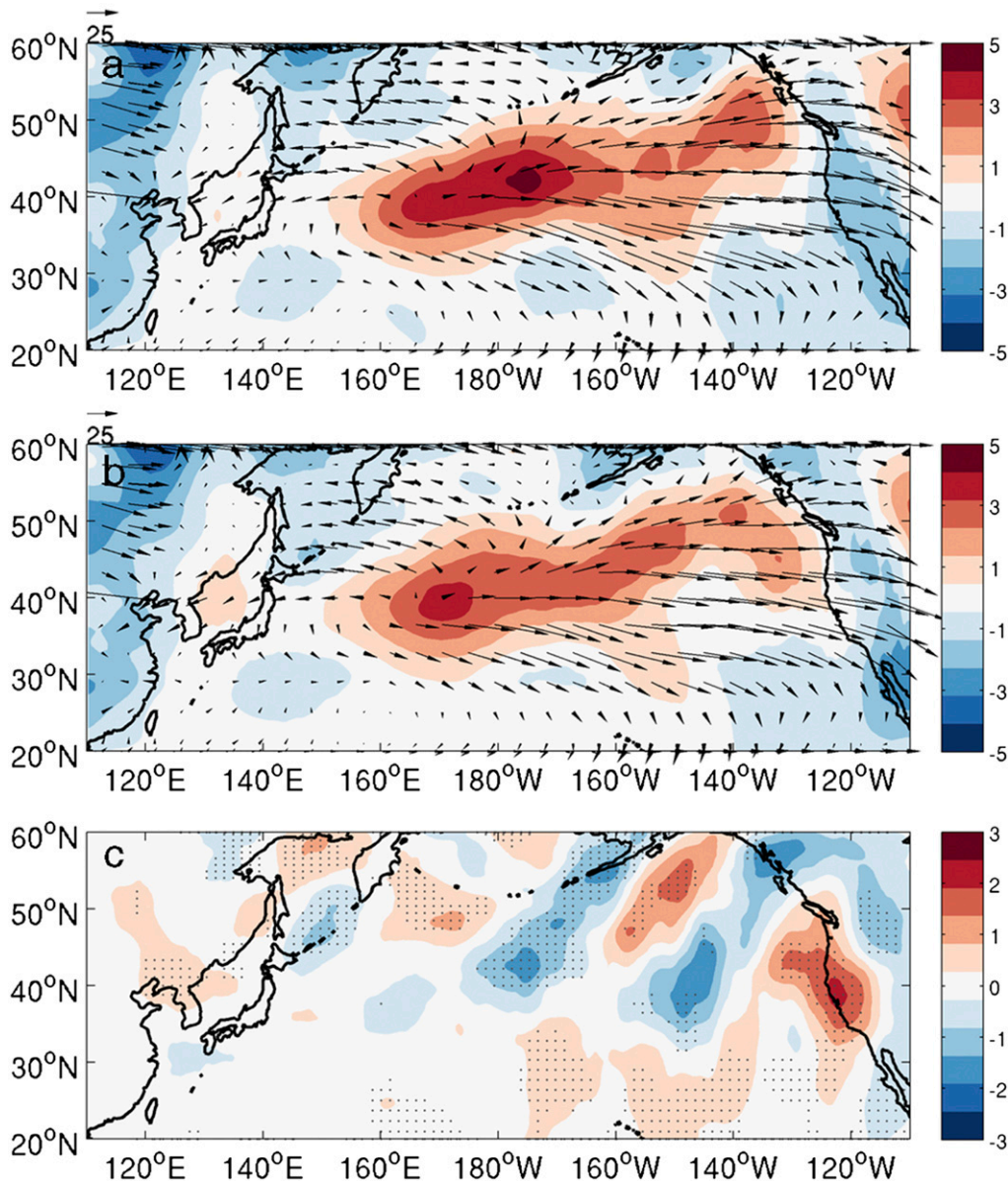


FIG. 11. Winter season (NDJFM) mean \mathbf{E} vector ($\text{m}^2 \text{s}^{-2}$; vectors) and $\nabla \cdot \mathbf{E}$ (10^{-5}m s^{-2} ; shaded) at 300 hPa simulated in (a) HR-CTRL and (b) HR-MEFS and (c) their difference. The difference significant at the 95% confidence level based on a two-sided Wilcoxon rank sum test is shaded by dots.

differences. It is evident that the stormy period GPH difference is much more pronounced than the less-stormy period difference. More interestingly, the stormy period GPH difference bears a remarkable resemblance, both in terms of shape and amplitude, to the winter mean GPH difference shown in Fig. 5g. In fact, the pattern correlation between the stormy period GPH difference (Fig. 12a) and winter mean GPH difference (Fig. 5g) is 0.96, and the former explains nearly 92% of the variance of the latter. On the other hand, the less-stormy period GPH difference contributes little to the winter mean GPH difference. These

results strongly suggest that the winter mean equivalent barotropic circulation anomaly that develops in the eastern North Pacific can be simply explained as the accumulative effect of the modified storm development caused by the absence of mesoscale SST forcing.

6. Conclusions and discussion

Ensembles of high (27 km) and low (162 km) resolution WRF simulations with and without mesoscale SST forcing are conducted during the boreal winter

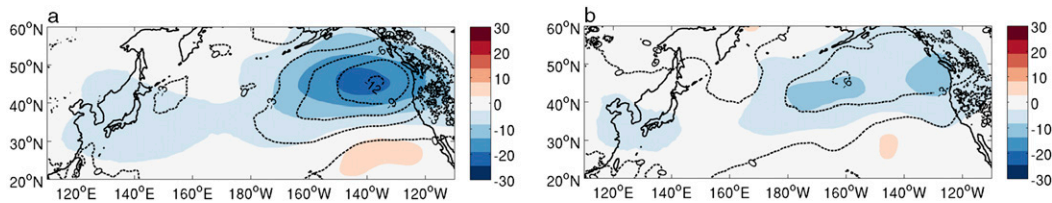


FIG. 12. Difference of Z850 (m; contours) and Z300 (m; color shaded) composite between HR-MEFS and HR-CTRL during the (a) stormy period and (b) less-stormy period. The stormy-day composite is calculated by summing up all the contribution of GPH anomalies during 4 days following the storm onset day. The less-stormy day composite is calculated by summing up the contribution from the remaining days.

(October–March) of 2007/08 to study the importance of resolving mesoscale oceanic eddies and diabatic heating process in accurately simulating cyclogenesis and storm-track variability in the North Pacific. In the high-resolution WRF simulations, removal of mesoscale SST forcing not only results in a significant reduction in cyclogenesis in the KER but also leads to a basin-scale equivalent barotropic response in the eastern North Pacific. Consistent with this response, a marked shift in the downstream storm track and mean flow is identified over the eastern North Pacific. In contrast, the low-resolution simulations produce a muted response in both KER cyclogenesis and downstream storm track/mean flow. This lack of robust response is not due to the weaker amplitude of mesoscale SST forcing in the low-resolution run but due to inadequate model resolution for resolving small-scale diabatic processes during cyclogenesis, as demonstrated by conducting another ensemble of low-resolution WRF runs where mesoscale SST forcing is amplified by 50%.

The dynamics behind the different local and remote atmospheric response to mesoscale SST forcing between high- and low-resolution simulations are investigated in depth. The local storm-track response in the high-resolution simulation is related to changes in cyclogenesis caused by mesoscale SST forcing through moist baroclinic instability. It is found that the presence of mesoscale SST forcing enhances diabatic energy conversion to EPE that in turn increases EPE-to-EKE conversion, leading to stronger storm growth in the KER and altered downstream storm development. The accumulative effect of the altered storm development contributes to the equivalent barotropic circulation response in the eastern North Pacific. In the low-resolution simulations, there is some evidence of local PBL response to mesoscale SSTs, but the diabatic energy conversion does not change significantly owing to the fact that narrow diabatic heating structures associated with cyclogenesis are not adequately resolved. This leads to the insignificant response of the storm track and large-scale atmospheric circulation to mesoscale SST

forcing, even when the SST forcing is amplified. These results indicate that in order to correctly simulate North Pacific storm-track variability, not only does mesoscale air–sea coupling associated with oceanic eddies need to be captured by climate models, but the small-scale diabatic heating associated with extratropical cyclogenesis also needs to be adequately resolved. In the current generation of global climate models with typical horizontal resolutions of $\sim 1^\circ$, neither mesoscale air–sea coupling nor diabatic heating is properly resolved, raising concerns about whether the extratropical cyclone and storm-track responses to midlatitude SST forcing are accurately simulated.

Identifying and quantifying Kuroshio eddies' effect on the Pacific storm track using available observations can be challenging and difficult at present because high-resolution data records required to resolve mesoscale SST variability and its coupling with the atmospheric circulation are short and limited. A few observational analyses have recently been carried out to investigate atmospheric response to Kuroshio Extension (KE) variability (e.g., O'Reilly and Czaja 2015; Revelard et al. 2016), but the primary focus of these studies was directed to the effect of SST gradient variability along the KE on the atmosphere. The result of these studies shows that a weaker KE SST gradient tends to correspond to a southward shift in the Pacific storm track. Since a weak SST gradient is typically accompanied by an unstable KE regime with strong eddy activity (Qiu and Chen 2005), the result of these observation-based studies is seemingly at odds with the model-based finding that shows a southward shift in the storm track in the absence of Kuroshio eddies. However, some cautionary notes are in order when making comparison between the observational and modeling results. First, the observational studies are based on KE indices designed to measure SST gradient changes, which may not be optimized to measure eddy activity, because the two, albeit related, are not exactly correlated. Therefore, the observational result obtained by O'Reilly and Czaja (2015) and Revelard et al. (2016) may be better interpreted as

Pacific storm-track response to changes in KE SST gradient, whereas the modeling result shown here highlights the effect of Kuroshio eddies on the storm track. In reality, SST gradient and eddies can simultaneously exert influence on cyclogenesis, but their effects may be counteractive. This is because a weak (strong) SST gradient tends to be associated with strong (weak) eddy activity; while the former tends to weaken (strengthen) atmospheric baroclinicity and thus cyclogenesis via dry baroclinic instability, the latter tends to strengthen (weaken) cyclogenesis via moist baroclinic instability. Therefore, the net effect will be determined by the relative intensity of these two factors, which further complicates the interpretation of the observational result, making it more difficult to directly compare the modeling and observational findings. Second, by experiment design, the remote influence from other ocean basins and tropics on the Pacific storm track is eliminated in the modeling study, owing to the treatment of lateral boundary conditions in ensemble simulations. As a result, the simulated storm-track response can be directly attributed to mesoscale SST forcing within the North Pacific basin. The observational studies attempted to filter the remote influence and internal variability using statistical means, but because of the limited sample size in the observations the storm-track response may still be contaminated by these influences, making it difficult to link the observed storm-track response to local SST forcing. Finally, until the observed atmospheric response to mesoscale SST forcing can be unambiguously quantified, one cannot exclude the possibility that the simulated storm-track response may not be a faithful representation of the real world. This issue can be partially addressed by conducting future modeling studies, including model sensitivity studies on physics parameterizations and intermodel comparison studies.

Acknowledgments. This research is supported by China's National Basic Research Priorities Program (2013CB956204), the National Natural Science Foundation of China (41490640, 41490643, 41490644, and 41306004). U.S. National Science Foundation Grants AGS-1067937 and AGS-1462127, and National Oceanic and Atmospheric Administration Grant NA11OAR4310154. XM acknowledges the support from the Chinese Scholarship Council. PC expresses his gratitude to the Japan Society for the Promotion of Sciences (JSPS) for a fellowship supporting his extended visit to the Research Center for Advanced Science and Technology at the University of Tokyo in 2015. We also thank Jeff Willison for providing the code of calculating diabatic heating in the WRF Model. The Texas Advanced Computing Center (TACC) at the University of Texas at Austin and the Texas A&M

Supercomputing Facility provided high-performance computing resources that contributed to the research results reported in this paper.

REFERENCES

- Ahmadi-Givi, F., G. C. Graig, and R. S. Plant, 2004: The dynamics of a midlatitude cyclone with very strong latent-heat release. *Quart. J. Roy. Meteor. Soc.*, **130**, 295–323, doi:[10.1256/qj.02.226](https://doi.org/10.1256/qj.02.226).
- Barsugli, J. J., and D. S. Battisti, 1998: The basic effects of atmosphere–ocean thermal coupling on midlatitude variability. *J. Atmos. Sci.*, **55**, 477–493, doi:[10.1175/1520-0469\(1998\)055<0477:TBOAO>2.0.CO;2](https://doi.org/10.1175/1520-0469(1998)055<0477:TBOAO>2.0.CO;2).
- Benedict, J. J., S. Lee, and S. B. Feldstein, 2004: Synoptic view of the North Atlantic Oscillation. *J. Atmos. Sci.*, **61**, 121–144, doi:[10.1175/1520-0469\(2004\)061<0121:SVOTNA>2.0.CO;2](https://doi.org/10.1175/1520-0469(2004)061<0121:SVOTNA>2.0.CO;2).
- Booth, J. F., L. A. Thompson, J. Patoux, K. A. Kelly, and S. Dickinson, 2010: The signature of the midlatitude tropospheric storm tracks in the surface winds. *J. Climate*, **23**, 1160–1174, doi:[10.1175/2009JCLI3064.1](https://doi.org/10.1175/2009JCLI3064.1).
- Brayshaw, D. J., B. Hoskins, and M. Blackburn, 2008: The storm-track response to idealized SST perturbations in an aquaplanet GCM. *J. Atmos. Sci.*, **65**, 2842–2860, doi:[10.1175/2008JAS2657.1](https://doi.org/10.1175/2008JAS2657.1).
- Bryan, F. O., R. Tomas, J. M. Dennis, D. B. Chelton, N. G. Loeb, and J. L. McClean, 2010: Frontal scale air–sea interaction in high-resolution coupled climate models. *J. Climate*, **23**, 6277–6291, doi:[10.1175/2010JCLI3665.1](https://doi.org/10.1175/2010JCLI3665.1).
- Chang, E. K. M., S. Y. Lee, and K. L. Swanson, 2002: Storm track dynamics. *J. Climate*, **15**, 2163–2183, doi:[10.1175/1520-0442\(2002\)015<0216:STD>2.0.CO;2](https://doi.org/10.1175/1520-0442(2002)015<0216:STD>2.0.CO;2).
- Chelton, D., and S.-P. Xie, 2010: Coupled ocean–atmosphere interaction at oceanic mesoscales. *Oceanography*, **23**, 52–69, doi:[10.5670/oceanog.2010.05](https://doi.org/10.5670/oceanog.2010.05).
- , M. G. Schlax, M. H. Freilich, and R. F. Milliff, 2004: Satellite measurements reveal persistent small-scale features in ocean winds. *Science*, **303**, 978–983, doi:[10.1126/science.1091901](https://doi.org/10.1126/science.1091901).
- Chou, M.-D., and M. J. Suarez, 1994: An efficient thermal infrared radiation parameterization for use in general circulation models. NASA Tech. Memo. 104606, 92 pp.
- Davis, C. A., and K. A. Emanuel, 1991: Potential vorticity diagnostics of cyclogenesis. *Mon. Wea. Rev.*, **119**, 1929–1953, doi:[10.1175/1520-0493\(1991\)119<1929:PVDOC>2.0.CO;2](https://doi.org/10.1175/1520-0493(1991)119<1929:PVDOC>2.0.CO;2).
- Dee, D. P., and Coauthors, 2011: The ERA-Interim reanalysis: Configuration and performance of the data assimilation system. *Quart. J. Roy. Meteor. Soc.*, **137**, 553–597, doi:[10.1002/qj.828](https://doi.org/10.1002/qj.828).
- Deser, C., G. Magnusdottir, R. Saravanan, and A. Phillips, 2004: The effects of North Atlantic SST and sea ice anomalies on the winter circulation in CCM3. Part II: Direct and indirect components of the response. *J. Climate*, **17**, 877–889, doi:[10.1175/1520-0442\(2004\)017<0877:TEONAS>2.0.CO;2](https://doi.org/10.1175/1520-0442(2004)017<0877:TEONAS>2.0.CO;2).
- Emanuel, K. A., M. Fantini, and A. J. Thorpe, 1987: Baroclinic instability in an environment of small stability to slantwise moist convection. 1. Two-dimensional models. *J. Atmos. Sci.*, **44**, 1559–1573, doi:[10.1175/1520-0469\(1987\)044<1559:BIIAEO>2.0.CO;2](https://doi.org/10.1175/1520-0469(1987)044<1559:BIIAEO>2.0.CO;2).
- Fay, M. P., and M. A. Proschan, 2010: Wilcoxon–Mann–Whitney or t-test? On assumptions for hypothesis tests and multiple interpretations of decision rules. *Stat. Surv.*, **4**, 1–39.
- Feldstein, S. B., 2003: The dynamics of NAO teleconnection pattern growth and decay. *Quart. J. Roy. Meteor. Soc.*, **129**, 901–924, doi:[10.1256/qj.02.76](https://doi.org/10.1256/qj.02.76).
- Frankignoul, C., 1985: Sea surface temperature anomalies, planetary waves, and air–sea feedback in the middle latitudes. *Rev. Geophys.*, **23**, 357–390, doi:[10.1029/RG023i004p00357](https://doi.org/10.1029/RG023i004p00357).

- , and K. Hasselmann, 1977: Stochastic climate models, part II: Application to sea-surface temperature anomalies and thermocline variability. *Tellus*, **29A**, 289–305, doi:[10.1111/j.2153-3490.1977.tb00740.x](https://doi.org/10.1111/j.2153-3490.1977.tb00740.x).
- , E. Kestenare, and J. Mignot, 2002: The surface heat flux feedback. Part II: direct and indirect estimates in the ECHAM4/OPA8 coupled GCM. *Climate Dyn.*, **19**, 649–655, doi:[10.1007/s00382-002-0253-9](https://doi.org/10.1007/s00382-002-0253-9).
- , N. Sennéchaël, Y.-O. Kwon, and M. A. Alexander, 2011: Influence of the meridional shifts of the Kuroshio and the Oyashio Extensions on the atmospheric circulation. *J. Climate*, **24**, 762–777, doi:[10.1175/2010JCLI3731.1](https://doi.org/10.1175/2010JCLI3731.1).
- Frenger, I., N. Gruber, R. Knutti, and M. Munnich, 2013: Imprint of Southern Ocean eddies on winds, clouds and rainfall. *Nat. Geosci.*, **6**, 608–612, doi:[10.1038/ngeo1863](https://doi.org/10.1038/ngeo1863).
- Haack, T., S. D. Burk, and R. M. Hodur, 2005: U.S. West Coast surface heat fluxes, wind stress, and wind stress curl from a mesoscale model. *Mon. Wea. Rev.*, **133**, 3202–3216, doi:[10.1175/MWR3025.1](https://doi.org/10.1175/MWR3025.1).
- Hasselmann, K., 1976: Stochastic climate models: Part I. Theory. *Tellus*, **28A**, 473–485, doi:[10.1111/j.2153-3490.1976.tb00696.x](https://doi.org/10.1111/j.2153-3490.1976.tb00696.x).
- Held, I. M., and B. J. Hoskins, 1985: Large-scale eddies and the general circulation of the troposphere. *Advances in Geophysics*, Vol. 28, Academic Press, 3–31, doi:[10.1016/S0065-2687\(08\)60218-6](https://doi.org/10.1016/S0065-2687(08)60218-6).
- Hong, S. Y., and H. L. Pan, 1996: Nonlocal boundary layer vertical diffusion in a medium-range forecast model. *Mon. Wea. Rev.*, **124**, 2322–2339, doi:[10.1175/1520-0493\(1996\)124<2322:NBLVDI>2.0.CO;2](https://doi.org/10.1175/1520-0493(1996)124<2322:NBLVDI>2.0.CO;2).
- Hoskins, B. J., and P. J. Valdes, 1990: On the existence of storm-tracks. *J. Atmos. Sci.*, **47**, 1854–1864, doi:[10.1175/1520-0469\(1990\)047<1854:OTEOST>2.0.CO;2](https://doi.org/10.1175/1520-0469(1990)047<1854:OTEOST>2.0.CO;2).
- , I. N. James, and G. H. White, 1983: The shape, propagation and mean-flow interaction of large-scale weather systems. *J. Atmos. Sci.*, **40**, 1595–1612, doi:[10.1175/1520-0469\(1983\)040<1595:TSPAMF>2.0.CO;2](https://doi.org/10.1175/1520-0469(1983)040<1595:TSPAMF>2.0.CO;2).
- Joyce, T. M., Y.-O. Kwon, and L. Yu, 2009: On the relationship between synoptic wintertime atmospheric variability and path shifts in the Gulf Stream and the Kuroshio Extension. *J. Climate*, **22**, 3177–3192, doi:[10.1175/2008JCLI2690.1](https://doi.org/10.1175/2008JCLI2690.1).
- Kain, J. S., 2004: The Kain–Fritsch convective parameterization: An update. *J. Appl. Meteor.*, **43**, 170–181, doi:[10.1175/1520-0450\(2004\)043<0170:TKCPAU>2.0.CO;2](https://doi.org/10.1175/1520-0450(2004)043<0170:TKCPAU>2.0.CO;2).
- Kanamitsu, M., W. Ebisuzaki, J. Woollen, S. K. Yang, J. J. Hnilo, M. Fiorino, and G. L. Potter, 2002: NCEP–DOE AMIP-II reanalysis (R-2). *Bull. Amer. Meteor. Soc.*, **83**, 1631–1643, doi:[10.1175/BAMS-83-11-1631](https://doi.org/10.1175/BAMS-83-11-1631).
- Kelly, K. A., R. J. Small, R. M. Samelson, B. Qiu, T. M. Joyce, Y.-O. Kwon, and M. F. Cronin, 2010: Western boundary currents and frontal air–sea interaction: Gulf Stream and Kuroshio Extension. *J. Climate*, **23**, 5644–5667, doi:[10.1175/2010JCLI3346.1](https://doi.org/10.1175/2010JCLI3346.1).
- Kushnir, Y., W. A. Robinson, I. Bladé, N. M. J. Hall, S. Peng, and R. Sutton, 2002: Atmospheric GCM response to extratropical SST anomalies: Synthesis and evaluation. *J. Climate*, **15**, 2233–2256, doi:[10.1175/1520-0442\(2002\)015<2233:AGRTE5>2.0.CO;2](https://doi.org/10.1175/1520-0442(2002)015<2233:AGRTE5>2.0.CO;2).
- Kwon, Y.-O., M. A. Alexander, N. A. Bond, C. Frankignoul, H. Nakamura, B. Qiu, and L. A. Thompson, 2010: Role of the Gulf Stream and Kuroshio–Oyashio systems in large-scale atmosphere–ocean interaction: A review. *J. Climate*, **23**, 3249–3281, doi:[10.1175/2010JCLI3343.1](https://doi.org/10.1175/2010JCLI3343.1).
- Lapeyre, G., and I. M. Held, 2004: The role of moisture in the dynamics and energetics of turbulent baroclinic eddies. *J. Atmos. Sci.*, **61**, 1693–1710, doi:[10.1175/1520-0469\(2004\)061<1693:TROMIT>2.0.CO;2](https://doi.org/10.1175/1520-0469(2004)061<1693:TROMIT>2.0.CO;2).
- Lin, Y. L., R. D. Farley, and H. D. Orville, 1983: Bulk parameterization of the snow field in a cloud model. *J. Appl. Meteor. Climatol.*, **22**, 1065–1092, doi:[10.1175/1520-0450\(1983\)022<1065:BPOTSF>2.0.CO;2](https://doi.org/10.1175/1520-0450(1983)022<1065:BPOTSF>2.0.CO;2).
- Ma, X., and Coauthors, 2015: Distant influence of Kuroshio eddies on North Pacific weather patterns? *Sci. Rep.*, **5**, 17785, doi:[10.1038/srep17785](https://doi.org/10.1038/srep17785).
- Mantua, N. J., S. R. Hare, Y. Zhang, J. M. Wallace, and R. C. Francis, 1997: A Pacific interdecadal climate oscillation with impacts on salmon production. *Bull. Amer. Meteor. Soc.*, **78**, 1069–1079, doi:[10.1175/1520-0477\(1997\)078<1069:APICOW>2.0.CO;2](https://doi.org/10.1175/1520-0477(1997)078<1069:APICOW>2.0.CO;2).
- Masunaga, R., H. Nakamura, T. Miyasaka, K. Nishii, and B. Qiu, 2016: Interannual modulations of oceanic imprints on the wintertime atmospheric boundary layer under the changing dynamical regimes of the Kuroshio Extension. *J. Climate*, **29**, 3273–3296, doi:[10.1175/JCLI-D-15-0545.1](https://doi.org/10.1175/JCLI-D-15-0545.1).
- Miller, A. J., and N. Schneider, 2000: Interdecadal climate regime dynamics in the North Pacific Ocean: Theories, observations and ecosystem impacts. *Prog. Oceanogr.*, **47**, 355–379, doi:[10.1016/S0079-6611\(00\)00044-6](https://doi.org/10.1016/S0079-6611(00)00044-6).
- Minobe, S., A. Kuwano-Yoshida, N. Komori, S. P. Xie, and R. J. Small, 2008: Influence of the Gulf Stream on the troposphere. *Nature*, **452**, 206–209, doi:[10.1038/nature06690](https://doi.org/10.1038/nature06690).
- Mlawer, E. J., S. J. Taubman, P. D. Brown, M. J. Iacono, and S. A. Clough, 1997: Radiative transfer for inhomogeneous atmospheres: RRTM, a validated correlated-k model for the longwave. *J. Geophys. Res.*, **102**, 16 663–16 682, doi:[10.1029/97JD00237](https://doi.org/10.1029/97JD00237).
- Nakamura, H., T. Sampe, A. Goto, W. Ohfuchi, and S.-P. Xie, 2008: On the importance of midlatitude oceanic frontal zones for the mean state and dominant variability in the tropospheric circulation. *Geophys. Res. Lett.*, **35**, L15709, doi:[10.1029/2008GL034010](https://doi.org/10.1029/2008GL034010).
- Nonaka, M., Y. Sasai, H. Sasaki, B. Taguchi, and H. Nakamura, 2016: How potentially predictable are midlatitude ocean currents? *Sci. Rep.*, **6**, 20153, doi:[10.1038/srep20153](https://doi.org/10.1038/srep20153).
- Okumura, Y., S. P. Xie, A. Numaguti, and Y. Tanimoto, 2001: Tropical Atlantic air–sea interaction and its influence on the NAO. *Geophys. Res. Lett.*, **28**, 1507–1510, doi:[10.1029/2000GL012565](https://doi.org/10.1029/2000GL012565).
- O’Neill, L. W., D. B. Chelton, and S. K. Esbensen, 2005: High-resolution satellite measurements of the atmospheric boundary layer response to SST variations along the Agulhas Return Current. *J. Climate*, **18**, 2706–2723, doi:[10.1175/JCLI3415.1](https://doi.org/10.1175/JCLI3415.1).
- O’Reilly, C. H., and A. Czaja, 2015: The response of the Pacific storm track and atmospheric circulation to Kuroshio Extension variability. *Quart. J. Roy. Meteor. Soc.*, **141**, 52–66, doi:[10.1002/qj.2334](https://doi.org/10.1002/qj.2334).
- Orlanski, I., 2008: The rationale for why climate models should adequately resolve the mesoscale. *High Resolution Numerical Modelling of the Atmosphere and Ocean*, K. Hamilton and W. Ohfuchi, Eds., Springer, 29–44.
- Park, S., C. Deser, and M. A. Alexander, 2005: Estimation of the surface heat flux response to sea surface temperature anomalies over the global oceans. *J. Climate*, **18**, 4582–4599, doi:[10.1175/JCLI3521.1](https://doi.org/10.1175/JCLI3521.1).
- Patricola, C. M., M. K. Li, Z. Xu, P. Chang, R. Saravanan, and J. S. Hsieh, 2012: An investigation of tropical Atlantic bias in a high-resolution coupled regional climate model. *Climate Dyn.*, **39**, 2443–2463, doi:[10.1007/s00382-012-1320-5](https://doi.org/10.1007/s00382-012-1320-5).

- , P. Chang, and R. Saravanan, 2016: Degree of simulated suppression of Atlantic tropical cyclones modulated by flavour of El Niño. *Nat. Geosci.*, **9**, 155–160, doi:[10.1038/ngeo2624](https://doi.org/10.1038/ngeo2624).
- Piazza, M., L. Terray, J. Boé, E. Maisonnave, and E. Sanchez-Gomez, 2016: Influence of small-scale North Atlantic sea surface temperature patterns on the marine boundary layer and free troposphere: A study using the atmospheric ARPEGE model. *Climate Dyn.*, **46**, 1699–1717, doi:[10.1007/s00382-015-2669-z](https://doi.org/10.1007/s00382-015-2669-z).
- Putrasahan, D. A., A. J. Miller, and H. Seo, 2013: Isolating meso-scale coupled ocean–atmosphere interactions in the Kuroshio Extension region. *Dyn. Atmos. Oceans*, **63**, 60–78, doi:[10.1016/j.dynatmoce.2013.04.001](https://doi.org/10.1016/j.dynatmoce.2013.04.001).
- Qiu, B., and S. Chen, 2005: Variability of the Kuroshio Extension jet, recirculation gyre, and mesoscale eddies on decadal time scales. *J. Phys. Oceanogr.*, **35**, 2090–2103, doi:[10.1175/JPO2807.1](https://doi.org/10.1175/JPO2807.1).
- , —, N. Schneider, and B. Taguchi, 2014: A coupled decadal prediction of the dynamic state of the Kuroshio Extension system. *J. Climate*, **27**, 1751–1764, doi:[10.1175/JCLI-D-13-00318.1](https://doi.org/10.1175/JCLI-D-13-00318.1).
- Revelard, A., C. Frankignoul, N. Sennechal, Y. O. Kwon, and B. Qiu, 2016: Influence of the decadal variability of the Kuroshio Extension on the atmospheric circulation in the cold season. *J. Climate*, **29**, 2123–2144, doi:[10.1175/JCLI-D-15-0511.1](https://doi.org/10.1175/JCLI-D-15-0511.1).
- Riviere, G., and I. Orlanski, 2007: Characteristics of the Atlantic storm-track eddy activity and its relation with the North Atlantic Oscillation. *J. Atmos. Sci.*, **64**, 241–266, doi:[10.1175/JAS3850.1](https://doi.org/10.1175/JAS3850.1).
- Saha, S., and Coauthors, 2010: The NCEP Climate Forecast System Reanalysis. *Bull. Amer. Meteor. Soc.*, **91**, 1015–1057, doi:[10.1175/2010BAMS3001.1](https://doi.org/10.1175/2010BAMS3001.1).
- Sampe, T., H. Nakamura, A. Goto, and W. Ohfuchi, 2010: Significance of a midlatitude SST frontal zone in the formation of a storm track and an eddy-driven westerly jet. *J. Climate*, **23**, 1793–1814, doi:[10.1175/2009JCLI3163.1](https://doi.org/10.1175/2009JCLI3163.1).
- Schlax, M. G., and D. B. Chelton, 1992: Frequency-domain diagnostics for linear smoothers. *J. Amer. Stat. Assoc.*, **87**, 1070–1081, doi:[10.1080/01621459.1992.10476262](https://doi.org/10.1080/01621459.1992.10476262).
- Seo, H., A. J. Miller, and J. O. Roads, 2007: The Scripps coupled ocean–atmosphere regional (SCOAR) model, with applications in the eastern Pacific sector. *J. Climate*, **20**, 381–402, doi:[10.1175/JCLI4016.1](https://doi.org/10.1175/JCLI4016.1).
- Skamarock, W. C., 2004: Evaluating mesoscale NWP models using kinetic energy spectra. *Mon. Wea. Rev.*, **132**, 3019–3032, doi:[10.1175/MWR2830.1](https://doi.org/10.1175/MWR2830.1).
- , and Coauthors, 2008: A description of the Advanced Research WRF version 3. NCAR Tech. Note NCAR/TN-475+STR, 113 pp., doi:[10.5065/D68S4MVH](https://doi.org/10.5065/D68S4MVH).
- Small, R. J., and Coauthors, 2008: Air–sea interaction over ocean fronts and eddies. *Dyn. Atmos. Oceans*, **45**, 274–319, doi:[10.1016/j.dynatmoce.2008.01.001](https://doi.org/10.1016/j.dynatmoce.2008.01.001).
- , R. A. Tomas, and F. O. Bryan, 2014: Storm track response to ocean fronts in a global high-resolution climate model. *Climate Dyn.*, **43**, 805–828, doi:[10.1007/s00382-013-1980-9](https://doi.org/10.1007/s00382-013-1980-9).
- Taguchi, B., H. Nakamura, M. Nonaka, and S.-P. Xie, 2009: Influences of the Kuroshio/Oyashio Extensions on air–sea heat exchanges and storm-track activity as revealed in regional atmospheric model simulations for the 2003/04 cold season. *J. Climate*, **22**, 6536–6560, doi:[10.1175/2009JCLI2910.1](https://doi.org/10.1175/2009JCLI2910.1).
- , —, —, N. Komori, A. Kuwano-Yoshida, K. Takaya, and A. Goto, 2012: Seasonal evolutions of atmospheric response to decadal SST anomalies in the North Pacific subarctic frontal zone: Observations and a coupled model simulation. *J. Climate*, **25**, 111–139, doi:[10.1175/JCLI-D-11-00046.1](https://doi.org/10.1175/JCLI-D-11-00046.1).
- Vallis, G. K., and E. P. Gerber, 2008: Local and hemispheric dynamics of the North Atlantic Oscillation, annular patterns and the zonal index. *Dyn. Atmos. Oceans*, **44**, 184–212, doi:[10.1016/j.dynatmoce.2007.04.003](https://doi.org/10.1016/j.dynatmoce.2007.04.003).
- Willison, J., W. A. Robinson, and G. M. Lackmann, 2013: The importance of resolving mesoscale latent heating in the North Atlantic storm track. *J. Atmos. Sci.*, **70**, 2234–2250, doi:[10.1175/JAS-D-12-0226.1](https://doi.org/10.1175/JAS-D-12-0226.1).
- Xie, S.-P., 2004: Satellite observations of cool ocean–atmosphere interaction. *Bull. Amer. Meteor. Soc.*, **85**, 195–208, doi:[10.1175/BAMS-85-2-195](https://doi.org/10.1175/BAMS-85-2-195).
- Zhou, G., M. Latif, R. J. Greatbatch, and W. Park, 2015: Atmospheric response to the North Pacific enabled by daily sea surface temperature variability. *Geophys. Res. Lett.*, **42**, 7732–7739, doi:[10.1002/2015GL065356](https://doi.org/10.1002/2015GL065356).